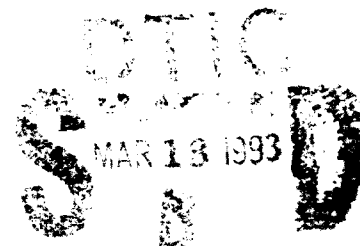


MML TR 93-04

ELECTROCHEMICAL BEHAVIOR AND SURFACE CHEMISTRY OF ALUMINUM
ALLOYS: SOLUTE-RICH INTERPHASE MODEL

Submitted to:

Office of Naval Research
800 North Quincy Street
Arlington, VA 22217-5000

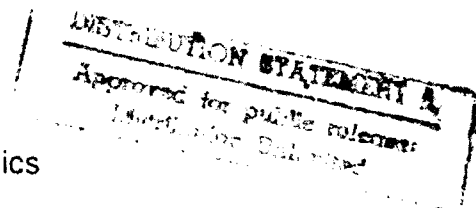


Submitted by:

G.D. Davis,* B.A. Shaw,† B.J. Rees,* E.L. Principe,† C.A. Pecile,† and A.S. Iyengar†

*Martin Marietta Laboratories
Baltimore, Maryland

†Department of Engineering Science and Mechanics
The Pennsylvania State University
University Park, Pennsylvania



March 1993

93-05548



Unclassified

SECURITY CLASSIFICATION OF THIS PAGE

REPORT DOCUMENTATION PAGE

1a REPORT SECURITY CLASSIFICATION Unclassified		1b RESTRICTIVE MARKINGS None									
2a SECURITY CLASSIFICATION AUTHORITY		3 DISTRIBUTION AVAILABILITY OF REPORT Unlimited									
2b DECLASSIFICATION/DOWNGRADING SCHEDULE None											
4 PERFORMING ORGANIZATION REPORT NUMBER(S) MML TR 93-04		5 MONITORING ORGANIZATION REPORT NUMBER(S)									
6a NAME OF PERFORMING ORGANIZATION Martin Marietta Corporation Martin Marietta Laboratories	6b OFFICE SYMBOL (If applicable) MML	7a NAME OF MONITORING ORGANIZATION Defense Contract Administration Services Management Area - Baltimore									
6c ADDRESS (City, State, and ZIP Code) 1450 South Rolling Road Baltimore, MD 21227-3898		7b ADDRESS (City, State, and ZIP Code) 300 East Joppa Road Baltimore, MD 21204-3099									
8a NAME OF FUNDING SPONSORING ORGANIZATION Office of Naval Research	8b OFFICE SYMBOL (If applicable) ONR	9 PROCUREMENT INSTRUMENT IDENTIFICATION NUMBER N00014-85-C-0638									
8c ADDRESS (City, State, and ZIP Code) 800 North Quincy Street Arlington, VA 22217-5000		10 SOURCE OF FUNDING NUMBERS <table border="1"> <tr> <td>PROGRAM ELEMENT NO</td> <td>PROJECT NO</td> <td>TASK NO</td> <td>WORK UNIT ACCESSION NO</td> </tr> <tr> <td></td> <td></td> <td></td> <td></td> </tr> </table>		PROGRAM ELEMENT NO	PROJECT NO	TASK NO	WORK UNIT ACCESSION NO				
PROGRAM ELEMENT NO	PROJECT NO	TASK NO	WORK UNIT ACCESSION NO								
11 TITLE (Include Security Classification) Electrochemical Behavior and Surface Chemistry of Aluminum Alloys: Solute-Rich Interphase Model											
12 PERSONAL AUTHOR(S) G.D. Davis, B.A. Shaw, B.J. Rees, E.L. Principe, C.a. Pecile, and A.S. Iyengar											
13a TYPE OF REPORT Annual	13b TIME COVERED FROM 12/1/91 TO 11/30/92	14 DATE OF REPORT (Year, Month, Day) March 31, 1993	15 PAGE COUNT 41								
16 SUPPLEMENTARY NOTATION											
17 COSAT CODES <table border="1"> <tr> <th>FIELD</th> <th>GROUP</th> <th>SUB-GROUP</th> </tr> <tr> <td></td> <td></td> <td></td> </tr> </table>		FIELD	GROUP	SUB-GROUP				18 SUBJECT TERMS (Continue on reverse if necessary and identify by block number) Approved for public release; distribution unlimited. Reproduction in whole or in part is permitted for any purpose of the United States Government.			
FIELD	GROUP	SUB-GROUP									
19 ABSTRACT (Continue on reverse if necessary and identify by block number) The electrochemical behavior of physical-vapor-deposited nonequilibrium stainless Al-W and Al-Ta alloys and the electrochemical behavior and surface chemistry of sputter-deposited nonequilibrium stainless Al-Ta alloys have been investigated. Results from the vapor-deposited alloys show that these materials possess enhanced passivity despite the presence of nodules and other defects. The stainless aluminum alloys that exhibit better performance are the sputter-deposited thin films that more uniform. Sputter-deposited Al-Ta alloys exhibit enhanced passivity over a pH range of 2 to 12 even though the passive film chemistry varies considerably over this range. This enhanced passivity can be explained by the solute-rich interphase model (SRIM), which claims that formation and passivation of occluded cells are controlled by localized concentrations of solute. The higher concentrations of solute at the metal-oxide interface and around occluded cells stabilize the passive film from continued chloride attack and dissolution.											
20 DISTRIBUTION AVAILABILITY OF ABSTRACT <input type="checkbox"/> UNCLASSIFIED UNLIMITED <input type="checkbox"/> SAME AS RPT <input type="checkbox"/> DTIC USERS		21 ABSTRACT SECURITY CLASSIFICATION Unclassified									
22 NAME OF PERSONS OR ORGANIZATION Dr. Guy D. Davis		23b TELEPHONE (Include Area Code) 410-204-2376	23c OFFICE SYMBOL								

INTRODUCTION

Aluminum and its conventional alloys are susceptible to localized attack in chloride-containing environments. Although the corrosion resistance of steels can be dramatically improved by the incorporation of chromium, molybdenum, and other elements to make stainless steels, there are no equivalent conventional stainless aluminum alloys. The failure to produce such alloys is largely due to the very low solubility of passivating species in aluminum; above a small fraction of an atomic percent, these species form precipitates, and microgalvanic couples established between the two phases can increase corrosion.

In the last several years, supersaturated aluminum alloys with Mo, Cr, Ta, W, Zr, Nb, Zn, V, Cu, Ti, and Si have been produced by several groups using rapid solidification or other nonequilibrium methods.[1-28] Several alloys have shown significant improvements in passivity in chloride-containing environments. For our sputter-deposited thin films, Al-W, Al-Ta, and Al-Mo alloys have shown the best performance with breakdown potentials well above 0 V (SCE) and passive regions exceeding 1000 mV.[4-9] All potentials given in this report are relative to a saturated calomel electrode (SCE).

During this contract year, we have continued to pursue two areas of investigation: production and testing of bulk or thick-film Al-Ta and Al-W material; and continued investigation of the mechanisms by which these stainless aluminum alloys exhibit enhanced passivity. Although thin films of stainless aluminum have potential applications in electronic devices and metal-matrix composites, bulk or thick-film material has even more potential applications. Accordingly, we have characterized and evaluated the corrosion performance of thick-film material produced by physical vapor deposition (PVD).

Several different mechanisms have been proposed to explain the passivity of stainless aluminum alloys, including electrostatic repulsion of Cl^- by oxidized solute atoms,[1-3] formation of an oxidized solute barrier layer,[3,4] blockage of Cl^- transport through the passive film,[19] stabilization of the passive film oxide structure,[6] replacement of oxidized Al in the passive film by oxidized solute to form a more stable oxide,[25,26] reduction of the acidification and dissolution within occluded cells,[17] and reduction in Cl^- adsorption due to pH_{pzc} changes.[11-17] Additionally, Macdonald and

coworkers [29,30] have proposed a solute-vacancy interaction model (SVIM) in which it is suggested that pits originate as vacancies collect at the metal/passive film interface, which causes the film to collapse locally; highly oxidized solute atoms form complexes with cation vacancies formed by Cl^- adsorption to reduce the diffusivity of the vacancies and slow their buildup at the metal/film interface.

Many of these mechanisms are variations and it is possible that different mechanisms may control the passivity of the various stainless aluminum alloys under different conditions. Very recently, we have proposed a solute-rich interphase model (SRIM) that incorporates various aspects of several models to explain the enhanced passivity of Al-W alloys [9]. We have continued to characterize and test stainless aluminum alloys under different conditions to further evaluate the mechanisms governing the passivity of these alloys and to determine the applicability of this model to other alloys. Specifically, we have examined the electrochemical behavior and, in some cases, the surface chemistry of Al-Ta alloys in KCl solutions of different pH values.

The behavior of these alloys at non-neutral pH values is of special interest since the Pourbaix diagrams for W and Ta and the literature for stainless steels suggest that the passivity of Al could be extended outside the pH range of 4 to 9 through the nonequilibrium addition of these elements to Al. Pourbaix diagrams for Al, W, and Ta are shown in Figure 1[31]. This figure reveals that passivity is anticipated at low pH values for W, at neutral pH values for Al, and over the entire range of pH values for Ta. It is reasonable to believe that the passivity of Al could be extended to lower pH values through the nonequilibrium addition of W and Ta. The literature for stainless steels [32-35] has shown that the addition of W (in the presence of a significant amount of Ni) enhances passivity at low pH values.

EXPERIMENTAL PROCEDURE

Thin-film Production

Thin-film specimens were produced by co-sputter deposition using a 602RS Loadlock thin film deposition system with both dc and RF magnetron sputtering.[36] Four-inch-diameter silicon wafers were mounted onto a rotating substrate holder to alleviate concentration gradients. These specimens were deposited at ambient tem-

peratures. Solute concentrations for the alloys were determined by induction coupled plasma (ICP); all concentrations are given in at.%. After deposition, the wafers were cleaved into smaller specimens for further evaluation.

Vapor Deposition

Two groups of vapor-deposited specimens were produced by Idaho National Engineering Laboratory (INEL) in 1992 -- one group (CD-12, CD-13, CD-16, and CD-17) was prepared in the winter and the second group (CD-25) was prepared in the fall. A schematic of the double source high-rate physical vapor deposition system used for producing the alloys appears in Figure 2. The flux from each source was independently controlled using a Telemark model 272 electron gun to obtain the desired alloy composition. Typical vacuum levels during deposition ranged from 10^{-2} to 10^{-3} Pa. To obtain a uniform deposit, the collector plate was rotated during deposition. Pure Al, W, or Ta were used as the sources and glass, aluminum, and silicon single-crystal wafers were used as collector plates.

X-ray Diffraction and Microscopy

Glancing angle x-ray diffraction (GXR), [37] with a constant angle of 10° between the incident x-ray beam and the film surface, was used to check the thin-film alloys for precipitate formation. The experiments were performed on a Scintag diffractometer using a monochromatic Cu K α x-ray source. The glancing angle was chosen both to optimize the signal from the metal film and to prevent diffraction from the Si single crystal.

All of the specimens were examined under an optical microscope before and after testing. Some of the specimens were examined using an ISI SS40 scanning electron microscope.

Electrochemical Experiments

Vapor-Deposited Alloys

Anodic potentiodynamic polarization experiments were performed on both groups of vapor-deposited specimens. These tests were conducted on EG&G Princeton Applied

Research potentiostats using Model 352 corrosion software. The specimens were tested in a flat cell (EG&G flat-cell model K0235), which simplified the mounting of the specimens since no lead wire attachment or coating of the specimens were required. The solutions were open to the atmosphere and not intentionally aerated or deaerated. Before polarization, the open circuit potentials were allowed to stabilize for 1 hour. Specimens were polarized at both the ASTM suggested slow scan rate of 0.2 mV/s and an even slower scan rate of 0.05 mV/s.

Thin-film Alloys

Individual electrochemical specimens were prepared by attaching a coated lead wire, and masking the back and edges of the specimens with a marine epoxy paint. Anodic potentiodynamic polarization curves were generated at a scan rate of 0.2 mV/s at ambient room temperature (23° to 27°C). A limited number of experiments were also run at a rate of 0.05 mV/s. All experiments were conducted on at least duplicate specimens in aerated chloride solutions with pH values ranging from 2 to 12 for the Al-Ta alloys. After immersion and before polarization, the open-circuit potentials, E_{OC} , were allowed to stabilize for at least 1 hour.

Surface Analysis

The chemistry of the Al-Ta passive film in pH 3 and pH 12 solutions was investigated in the as-sputtered condition, at the open circuit potential, and at various potentials up to E_b . The same specimens were repolarized until the breakdown potential was reached. Details of the procedure have been reported previously.[3,4] Changes in the surface chemistry induced by the transfer procedure and by exposure to ultrahigh vacuum have been examined and possible artifacts were shown to be either small (e.g., additional oxidation) or tractable (e.g., adventitious contamination), and differences in the measured surface chemistry were shown to originate in the electrolyte.[2,38]

The x-ray photoelectron spectroscopy (XPS) measurements were made using a Surface Science Instruments Model SSX 100-03 spectrometer with a monochromatized Al K α x-ray source and a hemispherical electron energy analyzer with multichannel detection. The x-ray source was focused to a spot size of 600 μ m and the surface charge was neutralized with low-energy electrons. Binding energies were normalized to that of adventitious hydrocarbon at 284.8 eV. Survey spectra provided a qualitative

analysis of the surface, whereas high-resolution spectra of the O 1s, C 1s, Al 2p, and Ta 4f photoelectron peaks were used for quantitative analysis and chemical state determination. Quantitative analysis data were obtained using peak areas and sensitivity factors determined from standards with our spectrometer. Chemical state separation was achieved by curve fitting, the details of which are presented elsewhere [3], with the Ta 4d doublet being constrained with a peak separation of 1.8 eV and an area ratio of 1.333.

The XPS data have been displayed in conventional representations and on surface behavior diagrams (SBD) [39,40] SBDs resemble ternary phase diagrams in that they represent a surface composition as a weighted sum of three basis compounds. However, they differ from phase diagrams in that surface compositional information rather than bulk phase information is represented. Furthermore, equilibrium condition is relaxed so that changes in the surface composition during nonequilibrium reactions can be traced.

SBDs have been used to trace the evolution of the surface composition during a variety of reactions with the environment [40-46] and as a function of depth into the material [47-50] The observed path can then be compared to paths predicted from proposed models and mechanisms. Often, the SBD representation allows insights not readily available from more conventional analyses. In the present case, the evolution of the passive film is traced as a function of overpotential for the different electrolytes.

The SBD was constructed by converting the atomic concentrations of oxidized Al, oxidized Ta, and O (following correction for the oxygen bound to adventitious hydrocarbon) to molar concentrations of Al_2O_3 , Ta_2O_5 , and H_2O . This linear transformation can be represented in matrix form as:

$$\begin{bmatrix} \text{Al}_2\text{O}_3 \\ \text{Ta}_2\text{O}_5 \\ \text{H}_2\text{O} \end{bmatrix} = k \begin{bmatrix} 1 & 0 & 0 \\ 0 & 1 & 0 \\ -3 & -5 & 1 \end{bmatrix} \begin{bmatrix} \text{Al} \\ \text{Ta} \\ \text{O} \end{bmatrix}$$

where $k=[2(\text{O}-2\text{Ta}-\text{Al})]^{-1}$ is a normalization factor.

Accession For	
NTIS GRA&I	<input checked="" type="checkbox"/>
DTIC TAB	<input type="checkbox"/>
Unannounced	<input type="checkbox"/>
Justification	
By	
Distribution/	
Availability Codes	
Dist	Avail. Codes
A-1	Special

RESULTS

Material Characterization -- Vapor-Deposited Materials

When observed under an optical microscope, the vapor-deposited alloys reveal numerous small nodules on their surfaces. The formation of these nodules from small fragments of the solute target was observed during the deposition process. It is believed that defects or impurities in the solute rod stock led to the ejection of these fragments of solute metal during electron-beam melting. These nodules are of concern for two reasons. First, depending on when the particles were ejected and whether they were subsequently coated with the alloy, their presence could establish localized galvanic couples on the surface leading to preferential dissolution of the alloy adjacent to these nodules. Second, the nodules disturb subsequent film growth; leading to the possible establishment of large, surface-connected defects in the deposit. Our earlier work revealed that small discontinuities in the substrate surface or small particles on the surface can have disastrous effects on alloy growth. Figure 3 shows a cross-section of vapor-deposited alloy that contained a small particle on the surface of the collector plate. This type of defect was noted using low-magnification microscopic evaluation of the alloy surfaces after deposition, as shown in Figure 4. In addition to acting as occluded cells, these sites could also have a negative influence on electrochemical test results by exposing the underlying collector plate to the test solution. Grain growth in the alloy was also found to be influenced by the presence of these nodules as Figure 5 illustrates.

X-ray diffraction of Al-W PVD alloys revealed the presence of WAl_{12} and possibly WAl_5 precipitates. At this point, it is uncertain whether these precipitates are associated with the nodules or the alloy. Fewer and/or smaller precipitates were also found in the Al-Ta alloys, but these have not yet been identified.

Electrochemical Experiments

Physical Vapor-Deposited Alloys

Electrochemical results for the various physical vapor-deposited alloys are listed in the Table 1. Despite the fact that the alloys contained numerous defects, quite promising corrosion performance was observed. As Table 1 reveals, the best results

were obtained for alloy CD-12 specimen No. 2 (Al-2.4%W), which exhibited a breakdown potential of -51 mV. This value is similar to the breakdown potentials reported earlier for our Al-1.5%W thin-film alloys. However, a replicate specimen from this same alloy showed a much lower breakdown potential of -479 mV, as shown in Figure 6. Note that the breakdown potential for pure Al is approximately -690 mV. Similar passive current densities were noted for all of the specimens. The large difference in the breakdown potential between the two replicate specimens is believed to be related to severe defects (probably surface connected) for the second specimen. Differences were also noted between replicate specimens for other compositions and at the slower potentiodynamic scan rate. Figures 7 to 10 show the behavior of replicate specimens for CD-13, CD-16, CD-17, and CD-25, respectively. A comparison of the behavior of Al-W alloys to that of pure Al is presented in Figure 11. All of the alloys show enhanced passivity in comparison to pure Al with the CD-12 and CD-25 specimens exhibiting the highest breakdown potentials. Because of the significant scatter between replicate specimens, no conclusions could be drawn regarding the influence of collector plate material on alloy performance. However, the smoothness and cleanliness of the surface, no matter what the substrate, were found to be critical factors in the deposition process.

Table 1. Anodic Polarization Data for Al-W and Al-Ta PVD Alloys in 0.1 M NaCl

SAMPLE	COMPOSITION	SCAN RATE (mV/s)	E _{oc} (mV)	E _b (mV)	i _p (μ A/cm ²)
CD12-1	Al-2.8W	0.2	-627	-479	0.148
CD12-2	Al-2.8W	0.2	-617	-51	0.107
CD13-3	Al-2.2Ta	0.2	-749	-303	0.314
CD13-4	Al-2.2Ta	0.2	-624	-102	0.634
CD16-10	Al-2.4Ta	0.2	-994	-415	0.997
CD16-11	Al-2.4Ta	0.2	-927	-375	0.134
CD17A-1	Al-1.9W	0.2	-686	-480	0.34
CD17A-2	Al-1.9W	0.2	-683	-580	0.599
CD17B-1	Al-1.9W	0.2	-660	Active	Active
CD17B-2	Al-1.9W	0.2	-672	-531	0.464
CD25-1	Al-3.8W	0.2	-613	-365	0.295
CD25-2	Al-3.8W	0.2	-715	-463	0.117
CD25-4	Al-3.8W	0.05	-759	-441	0.123
CD25-5	Al-3.8W	0.05	-676	-311	0.194

Thin-film Alloys

Anodic potentiodynamic polarization was conducted on 24 Al-Ta thin-film specimens. These experiments were carried out at a variety of pH values and at two different scan rates, as outlined in Table 2. Deaerated solutions were used for most of the experiments and the Ta concentration in the alloy was 2.8%. Polarization data for pure bulk Al and Ta are also presented in Table 2.

Table 2. Polarization Data for Al-Ta Alloys in 0.1M NaCl

COMPOSITION	pH	DEAERATED	SCAN RATE (mV/s)	E _{oc} (mV)	E _b (mV)	i _p (μ A/cm ²)
Al-2.8Ta	12	N	0.2	-1207	1000	6
Al-2.8Ta	12	N	0.2	-1272	1000	1.8
Al-2.8Ta	12	Y	0.2	-1100	N/A	1.4
Al-2.8Ta	12	Y	0.2	-1112	950	2.3
Al-2.8Ta	12	Y	0.2	-1140	1100	2.2
Al-2.8Ta	12	Y	0.05	-1297	22	1.9
Al-2.8Ta	12	Y	0.05	-1451	213	1.3
Al-2.8Ta	12	Y	0.05	-1307	397	1.5
Al-2.8Ta	8	Y	0.05	-1324	-180	3.7
Al-2.8Ta	8	Y	0.05	-1316	92	0.71
Al-2.8Ta	2	Y	0.2	-837	Active	Active
Al-2.8Ta	2	Y	0.2	-839	Active	Active
Al-2.8Ta	2	Y	0.05	-972	-300	* 41.7
Al-2.8Ta	2	Y	0.05	-870	-277	* 6.6
Bulk Ta	12	Y	0.2	-130	> 1200	6.3
Bulk Ta	12	Y	0.2	-493	> 1200	1.6
Bulk Ta	12	Y	0.2	-515	> 1200	1.5
Bulk Ta	2	Y	0.2	-327	> 1200	1.5
Bulk Al	12	Y	0.2	-1322	-588	186
Bulk Al	2	Y	0.2	-675	Active	Active
Bulk Al	2	Y	0.2	-687	-628	* 0.73
Bulk Al	2	Y	0.2	-745	-630	* 4.5

* Average current density; current density is potential-dependent.

Polarization curves for duplicate Al-2.8Ta alloys in a pH 12 chloride solution (0.1M NaCl with the pH adjusted with NaOH) generated at a scan rate of 0.2 mV/s are presented in Figure 12. Reproducible behavior was observed with both curves exhibiting similar passive current densities and corrosion potentials. A slight perturbation in the current was observed at low potentials. This may indicate that the specimen had not reached steady state conditions. The most striking feature noted in

these curves was the high breakdown potential at approximately 800 mV. A comparison of the polarization behavior for this alloy with that of pure bulk Al and pure bulk Ta is shown in Figure 13. This comparison reveals that the Al-Ta alloy behavior is more like that of pure Ta than pure Al; suggesting that the passive film chemistry at pH 12 may be closer to that which forms on pure Ta. Indeed, XPS measurements indicate this to be the case.

Similar experiments were also conducted in a pH 2 chloride solution (0.1 M NaCl with the pH adjusted to 2). Replicate curves showed reproducible behavior; however, the behavior was quite different from that observed at the high pH. A comparison of the polarization behavior (generated at a scan rate of 0.2 mV/s) for the Al-Ta alloy with that of the pure metals in the pH 2 solution is shown in Figure 14. In this case, the alloy curve shows little evidence of passivity. The polarization curve for the Al-Ta alloy at low pH is similar to the curve generated for pure Al.

To confirm the results of these experiments, we conducted a series of anodic polarizations at a lower scan rate, 0.05 mV/s. A comparison of the 0.2 mV/s scan rate data with the data obtained at 0.05 mV/s, at a pH of 12, is presented in Figure 15. Our experiment revealed a much lower breakdown potential for the alloy at the slow scan rate and is consistent with the argument that the faster scan rate in this case does not allow sufficient time for breakdown of passivity to occur. One of the three curves generated for the Al-Ta alloy at a pH of 12 appears in Figure 15. Replicate curves at pH 12, generated at the slower scan rate, are presented in Figure 16. Breakdown potentials ranging from 22 mV to 397 mV and passive current densities of 1 to 2 $\mu\text{A}/\text{cm}^2$ were observed for these specimens. Some variation in the breakdown potential is expected since pitting is a stochastic process. In addition, small flaws in the alloy film have also been found to contribute to variations noted in the breakdown potential for these type of alloys. The slight perturbation in current at low overpotentials, which was noted at the faster scan rate, was not observed in any of the specimens tested at the lower scan rate.

At a pH of 2, the slower scan rate data for the Al-Ta alloy actually look better than the faster scan rate data, as Figure 17 illustrates. A more defined passive region and a more distinct breakdown potential are noted at the slower scan rate. An explanation for this behavior is presented in discussion section.

Al-Ta alloy polarization behavior was also evaluated at the 0.05 mV/s scan rate at a pH of 8. Behavior at this pH was similar to that observed at pH 12; however, a slightly lower breakdown potential was observed at pH 8. Figure 18 shows the polarization curves generated at pH 8 at the slower scan rate. A difference of 270 mV was noted in the breakdown potential and a variation in i_p from 0.7 to 3.7 $\mu\text{A}/\text{cm}^2$ was observed. Earlier polarization results for this alloy (without deaeration and with a scan rate of 0.2 mV/s) are also included in Table 2 and reveal i_p values similar to those observed at the faster scan rate and slightly lower breakdown potentials.

A comparison of the Al-Ta alloy polarization behavior as a function of pH is presented in Figure 19. Three observations can be made from these data. First, the open circuit potential increases as the pH decreases. This is expected since the potential of the hydrogen reduction reaction is potential dependent. Second, the breakdown potential increases with increasing pH and constant chloride concentration. Third, the passive current density increases with decreasing pH. An explanation for these last two observations is presented as part of the Discussion section.

Surface Analysis

The passive film chemistry of Al-Ta alloys depends strongly on the pH of the solution, especially in the near-neutral to basic solution range (Figure 20). As previously reported [4], in near-neutral solutions, the passive film remains thin (<10 nm) throughout the polarization sequence with the substrate being easily detected by XPS even at the breakdown potential. Considerable amounts of oxidized Ta are present open circuit potential (~20 percent of the oxidized cations); this composition remains essentially constant for the first 600 mV of polarization (Figure 21). Above this potential (corresponding to the potential at which pure aluminum pits), the oxidized Ta increases until the passive film contains nearly equal amounts of oxidized Ta and Al.

The behavior of the passive film in pH 3 solutions is generally similar. The film remains thin until the breakdown potential is reached. Although little Ta is found in the passive film at open circuit and the first polarization, its concentration increases with overpotential (Figure 21). At the breakdown potential, the passive film also contains comparable amounts of oxidized Al and Ta. Nonetheless, at the same overpotential, more oxidized Ta is found in the passive film formed at pH 3 than in that formed at pH 8.

The passive film formed in pH 12 solutions is very different. Even at the open circuit potential, the film is thicker than the information depth of XPS (~10 nm) and is composed entirely of oxidized Ta with no Al detected (Figure 21). Based on XPS quantitative analysis, the film is a hydrated form of Ta_2O_5 , $\text{Ta}(\text{OH})_5$. No change in the chemistry is observed during the polarization sequence.

Although Figures 20 and 21 are helpful in showing some of the differences and changes in passive film chemistry that occur during polarization for the three pH regions, the Al_2O_3 - Ta_2O_5 - H_2O SBD (Fig. 22) provides a more comprehensive understanding of the passive film evolution. In the deaerated pH 8 KCl solution, the film is initially partially hydrated Al_2O_3 (with a composition midway between Al_2O_3 and AlOOH) with 10 to 15 molar percent of Ta_2O_5 . The composition does not change until the breakdown potential of pure Al, E_b^{Al} , in this solution is reached when the concentration of Ta_2O_5 approximately doubles and some dehydration of the Al oxide occurs (path a). Upon further polarization in the regime where the Al-Ta alloys exhibit enhanced passivity, the film evolves along a line directly toward $\text{Ta}(\text{OH})_5$ (path b). That is, the $\text{Ta}_2\text{O}_5/\text{Al}_2\text{O}_3$ of the E_b^{Al} film is replaced by $\text{Ta}(\text{OH})_5$ as the Al^{+3} goes into solution and the Ta_2O_5 hydrates. As E_b is approached, more of the remaining Ta_2O_5 may undergo hydration with little change in the Al_2O_3 content and, thus, the evolution line in the SBD curves downward.

The evolution of the passive film chemistry in the aerated pH 3 solution is a less complex single-step process. The open circuit film is composed of Al_2O_3 with little or no hydration. Upon polarization, the film chemistry proceeds directly toward the $\text{Ta}(\text{OH})_5$ point of the SBD (path c), indicating a simple replacement of the Al_2O_3 with $\text{Ta}(\text{OH})_5$ as Al^{+3} goes into solution. Thus, the evolution of the passive film chemistry in the pH 3 solution is very similar to that occurring in the second phase at pH 8 -- an increase in the $\text{Ta}(\text{OH})_5$ concentration at the expense of the original constituents. At E_b , this replacement has progressed further so this film contains more $\text{Ta}(\text{OH})_5$ than the pH 8 film.

The evolution of the pH 12 passive film is also included in the SBD for completeness, but is less interesting. The film is composed of $\text{Ta}(\text{OH})_5$ from the open circuit to breakdown. (The small variation about the $\text{Ta}(\text{OH})_5$ point represents scatter in the data.)

DISCUSSION

To explain the enhanced passivity of Al-W alloys over a wide range of pH values despite large changes in the composition of the passive film, we have introduced the solute-rich interphase model [9]. The SRIM requires that the solute exhibit passivity (or, possibly, immunity) in the low-pH environment of an occluded cell or protopit. In this model, localized increases in the solute concentration at the metal-oxide interphase and at defects inhibit pit initiation and stabilize the occluded cells. If a defect in the passive film extends to the interphase, the solute-rich metal region below the film inhibits pit formation by forming an oxidized solute barrier layer and reduces Cl^- adsorption by locally reducing the pH_{pzc} (Fig. 23). If Al dissolution and acidification begin, the local solute concentration in both the alloy and passive film increases further (Fig. 23). The oxidized solute (a combination of WO_2 and WO_3 or, more likely based on quantitative XPS, $\text{W}(\text{OH})_4$ and $\text{W}(\text{OH})_6$) is more stable at the low pH environment of the pit than the original film, and the solute passivates the site. Passivity is further enhanced because, according to the pH_{pzc} model [11-15], less Cl^- would adsorb locally.

The SRIM predicts that increasing amounts of oxidized solute would be found in the passive film with greater overpotential as the density of passivated pits increases. The model also explains the correlation of E_b with the pH_{pzc} of the oxidized solute [15] despite the wide range of solute concentration in the passive film seen for different alloys under different conditions. The important factor is the solute's localized concentration in an occluded cell, not the overall concentration of the solute in the passive film. Because the film in such a cell is predominately oxidized solute, the local pH_{pzc} would be considerably lower than that of the passive film away from a cell.

The Pourbaix diagram for Ta also predicts passivity at low pH [31], suggesting that the SRIM might be applicable in the Al-Ta case as well. The evolution of the passive film chemistry in the SBD of Figure 22 indicates that this model can indeed explain the enhanced passivity of Al-Ta alloys. The pH 3 data show that $\text{Ta}(\text{OH})_5$, a hydrated form of oxidized Ta, is the passivating species under these conditions. As the specimen is polarized, the passive film evolves directly toward $\text{Ta}(\text{OH})_5$ (path c) as this species replaces the original oxidized Al. In deaerated pH 8 solutions, the passive film initially is a mixture of partially hydrated Al_2O_3 and Ta_2O_5 , both of which are stable species under these conditions. Little change in the composition is noted until E_b^{Al} is approached and the amount of Ta_2O_5 increases two-fold. Once E_b^{Al} is exceeded and

the alloy exhibits enhanced passivity, the amount of $\text{Ta}(\text{OH})_5$ increases as it replaces the $\text{Ta}_2\text{O}_5/\text{Al}_2\text{O}_3$ in the occluded cells and they passivate. Because the area of passivated pits is less than the total area even at E_b of the alloy, the passive film contains more oxidized Al than that of the pH 3 solution, which partially simulates the occluded cell environment.

This model is consistent with the changes observed in the polarization data for the Al-Ta alloy as a function of scan rate and pH. At pH 12 a lower breakdown potential was observed at the slower (0.05mV/s) scan rate. This is in line with the concept that slower scan rates allow more time for Cl^- to penetrate the passive film. Several possible routes for the Cl^- to reach the underlying metal have been proposed, including existing defects in the film, coalescence of cation vacancies [29,30], and fibrils [19]. At this high pH, the passive film for the alloy is entirely oxidized Ta with no Al detected -- the same chemistry as would be expected for a pure Ta substrate. However, unlike the case of pure Ta, a breakdown potential is observed for the Al-Ta alloys. This occurs when the Cl^- reaches the substrate (irrespective of how it got there) and finds the metal to be Al and not Ta. At this pH, the passive film is thicker than at the lower pH values and no Al is present. The low passive current density would be consistent with very limited dissolution of Ta through the $\text{Ta}(\text{OH})_5$ barrier.

At low pH, the passive film chemistry is similar to that observed at neutral pH -- oxidized Al and oxidized Ta are both present and the film is relatively thin (< 10nm). The increase in E_b with decreasing scan rate can be explained by considering competition between growth of the solute-rich interphase and an increased driving force for Cl^- to react with the metal as the potential is increased. With the slower scan rate more time is available for the solute-rich layer to develop and thus, a higher driving force is required for the Cl^- to interact with the metal. The higher passive current density at the lower pH can be explained by increased Al^{+3} dissolution from the pH-3 passive film as evidenced by the greater concentration of oxidized Ta at a given overpotential.

CONCLUSIONS

Several conclusions can be drawn from the data presented here that elucidate the mechanisms of passivity of nonequilibrium stainless aluminum alloys and identify alternative production methods.

Thick films of stainless aluminum that are grown by high-rate physical vapor deposition exhibit enhanced passivity despite nodules and other defects.

Thin-film Al-Ta alloys exhibit enhanced passivity over a wide range of pH values.

The passivating species of the Al-Ta alloys is $\text{Ta}(\text{OH})_5$, a hydrated form of oxidized Ta, as determined by quantitative XPS and surface behavior diagrams.

The concentration of $\text{Ta}(\text{OH})_5$ in the passive film is dependent on solution pH and increases with overpotential in pH 3 and pH 8 solutions.

The solute-rich interphase model (SRIM) previously developed for stainless Al-W alloys can also explain the enhanced passivity of Al-Ta alloys.

ACKNOWLEDGEMENTS

We gratefully acknowledge the contributions of G. Korth in providing the PVD specimens and of W.C. Moshier and R.G. Wendt in providing the thin-film Al-2.8Ta specimens.

REFERENCES

1. W.C. Moshier, G.D. Davis, J.S. Ahearn, and H.F. Hough, J. Electrochem. Soc. **133**, 1063 (1986).
2. W.C. Moshier, G.D. Davis, J.S. Ahearn, and H.F. Hough, J. Electrochem. Soc. **134**, 2677 (1987).
3. W.C. Moshier, G.D. Davis, and G.O. Cote, J. Electrochem. Soc. **136**, 356 (1989).
4. G.D. Davis, W.C. Moshier, T.L. Fritz, and G.O. Cote, J. Electrochem. Soc. **137**, 422 (1990).
5. B.A. Shaw, T.L. Fritz, G.D. Davis, and W.C. Moshier, J. Electrochem. Soc. **137**, 1317 (1990).
6. G.D. Davis, W.C. Moshier, G.G. Long, and D.R. Black, J. Electrochem. Soc. **138**, 3194 (1991).
7. B.A. Shaw, G.D. Davis, T.L. Fritz, B.J. Rees, and W.C. Moshier, J. Electrochem. Soc. **138**, 3288 (1991).

8. B.A. Shaw, G.D. Davis, T.L. Fritz, B.J. Rees, and W.C. Moshier, in *Critical Factors in Localized Corrosion*, G.S. Frankel and R.C. Newman, eds. (The Electrochemical Society, Pennington, NJ, 1992), p. 323.
9. G.D. Davis, B.A. Shaw, B.J. Rees, and M. Ferry, *J. Electrochem. Soc.* **140**, 951 (1993).
10. T.R. Schrecengost, B.A. Shaw, and R.G. Wendt, W.C. Moshier, submitted to *Corros.*
11. P.M. Natishan, E. McCafferty, and G.K. Hubler, *J. Electrochem. Soc.* **133**, 1061 (1986).
12. E. McCafferty, G.K. Hubler, P.M. Natishan, P.G. Moore, R.A. Kant, and B.D. Sartwell, *Mater. Sci. Eng.* **86**, 1 (1987).
13. P.M. Natishan, E. McCafferty, and G.K. Hubler, *J. Electrochem. Soc.* **135**, 321 (1988).
14. P.M. Natishan, E. McCafferty, and G.K. Hubler, *Corros. Sci.* **32**, 721 (1991).
15. E. McCafferty and P.M. Natishan, in *Critical Factors in Localized Corrosion*, G.S. Frankel and R.C. Newman eds. (The Electrochemical Society, Pennington, NJ, 1992), p. 299..
16. G.S. Frankel, M.A. Russak, C.V. Jahnes, M. Mirzamaani, and V.A. Brusic, *J. Electrochem. Soc.* **136**, 1243 (1989).
17. Z. Szklarska-Smialowska, in *Critical Factors in Localized Corrosion*, G.S. Frankel and T.C. Newman, eds. (The Electrochemical Society, Pennington, NJ, 1992), p. 311.
18. R.C. Bhardwaj, A. González-Martín, and J. O'M. Bockris, *J. Electrochem. Soc.* **139**, 1050 (1992).
19. J. O'M. Bockris and Lj. V. Minevski, accepted by *J. Appl. Electrochem.*
20. A. González-Martín, R.C. Bhardwaj, and J. O'M. Bockris, accepted by *J. Electrical Anal. Chem.*
21. A.H. Al-Saffar, V. Ashworth, A.K.O. Vairamov, D.J. Chivers, W.A. Grant, R.P.M. Procter, *Corros. Sci.* **20**, 127 (1980).
22. M.V. Zeller and J.A. Kargol, *Appl. Surf. Sci.* **18**, 63 (1984).
23. R.W. Gardiner and M.C. McConnell, *Met. Mater.* **3**, 254 (1987)
24. M. Fass, D. Itzhak, D. Eliezer, F.H. Froes, *J. Mater. Sci. Lett.* **6**, 1227 (1987).
25. H. Yoshioka, H. Habazaki, A. Kawashima, K. Asami, and K. Hashimoto, *Corros. Sci.* **32**, 313 (1991).

26. H. Yoshioka, A. Kawashima, K. Asami, and K. Hashimoto, in *Proc. Symp. Corrosion, Electrochemistry, and Catalysis of Metallic Glasses* R.B. Diegle and K. Hashimoto, eds. (The Electrochemical Society, Pennington, NJ 1988) p. 242.
27. F.G. Schenk, "The Influence of Heat Treatment on the Performance of Highly Corrosion Resistant Al Alloys," Trident Scholar Report No. 197, U.S. Navy Academy, 1992.
28. C.C. Streinz, "A Microellipsometric Study of the Passive Film Formation on Solid Solution Al-Ta Alloys and the Role of Al₃Ta Precipitates in Breakdown," The Johns Hopkins University, Baltimore, MD (1992).
29. M. Urguidi and D.D. Macdonald, *J. Electrochem. Soc.* **132**, 555 (1985)
30. D.D. Macdonald, *J. Electrochem. Soc.* **139**, 3434 (1992).
31. M. Pourbaix, *Atlas of Electrochemical Equilibria in Aqueous Solutions*, (NACE, Houston, TX 1974) p. 168.
32. N. Bui, A. Irhzo, F. Dabosi, and Y. Limouzin-Maire, *Corros.* **39**, 491 (1983).
33. A. Irhzo, Y. Segui, N. Bui, and F. Dabosi, *Corros. Sci.* **26**, 769 (1986).
34. H. Habazaki, A. Kawashima, Kasami, and K. Hashimoto, in *The Applications of Surface Analysis Methods to Environmental/Material Interactions* (PV 91-7) D.R. Baer, C.R. Clayton, and G.D. Davis, eds., (The Electrochemical Society, Pennington, NJ, 1991) p. 467.
35. J. Chen and J.K. Wu, *Corros. Sci.* **30**, 53 (1990).
36. B.A. Shaw, T.R. Schrecengost, W.C. Moshier, and R.G. Wendt, "Inhibiting Corrosion in Gr/Al and Gr/Mg Metal Matrix Composites Using Nonequilibrium Alloying Techniques," Penn State Report to ONR, June 1992.
37. M. Nathan, *Mater. Lett.* **3**, 319 (1985).
38. G.D. Davis, W.C. Moshier, J.S. Ahearn, H.F. Hough and G.O. Cote, *J. Vac. Sci. Technol. A* **5**, 1152 (1987).
39. G.D. Davis, *Surf. Interface Anal.* **9**, 421 (1986).
40. G.D. Davis, T.S. Sun, J.S. Ahearn, and J.D. Venables, *J. Mater. Sci.* **17**, 1807 (1982).
41. G.D. Davis, J.S. Ahearn, and J.D. Venables, *J. Vac. Sci. Technol. A* **2**, 763 (1984).
42. G.D. Davis, J.S. Ahearn, L.J. Matienzo, and J.D. Venables, *J. Mater. Sci.* **20**, 975 (1985).
43. W.C. Moshier, G.D. Davis, and J.S. Ahearn, *Corros. Sci.* **27**, 785 (1987).
44. G.D. Davis, W.C. Moshier, J.S. Ahearn, H.F. Hough, and G.O. Cote, *J. Vac. Sci. Technol. A* **5**, 1152 (1987).
45. J.S. Ahearn and G.D. Davis, *J. Adhes.* **28**, 75 (1989).

46. V.P. Thompson, T.L. Edler, and G.D. Davis, *J. Adhes.* **39**, 157 (1992).
47. G.D. Davis, S.P. Buchner, W.A. Beck, and N.E. Byer, *Appl. Surf. Sci.* **15**, 238 (1983).
48. G.D. Davis, N.E. Byer, R.A. Riedel, and G. Margaritondo, *J. Appl. Phys.* **57**, 1915 (1985).
49. G.D. Davis, W.A. Beck, M.K. Kelly, D. Kilday, Y.W. Mo, N. Tache, and G. Margaritondo, *Phys. Rev. B.* **38**, 9694 (1988).
50. J.C. Bierlein, S.W. Gaarenstroom, R.A. Waldo, and A.C. Ottolini, *J. Vac. Sci. Technol. A* **2**, 1102 (1984).

Pourbaix Diagrams

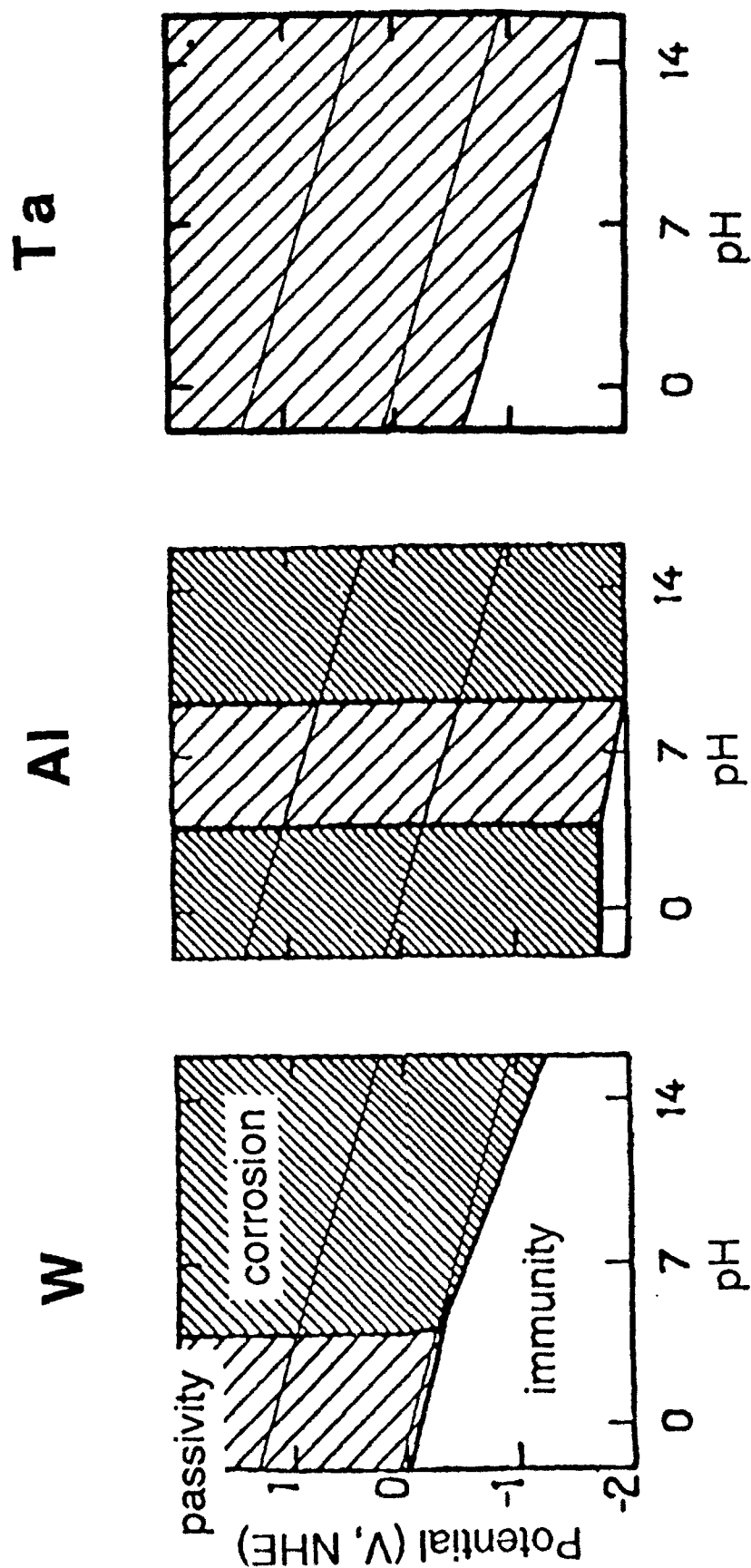


Figure 1. Pourbaix diagrams for Al, W, and Ta (Ref. 31).

Schematic of High-Rate PVD System

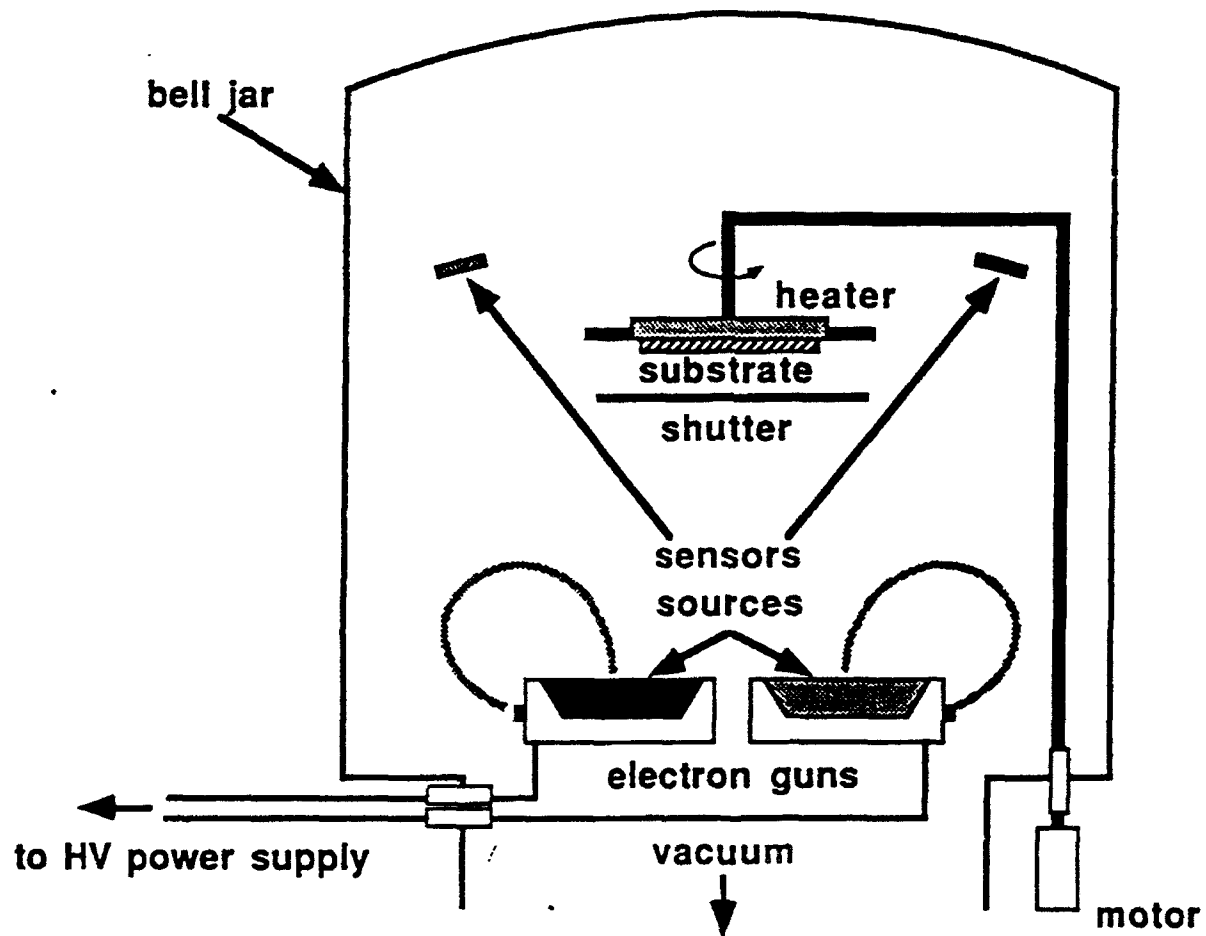


Figure 2. Schematic diagram of High-Rate Physical Vapor-Deposition System.

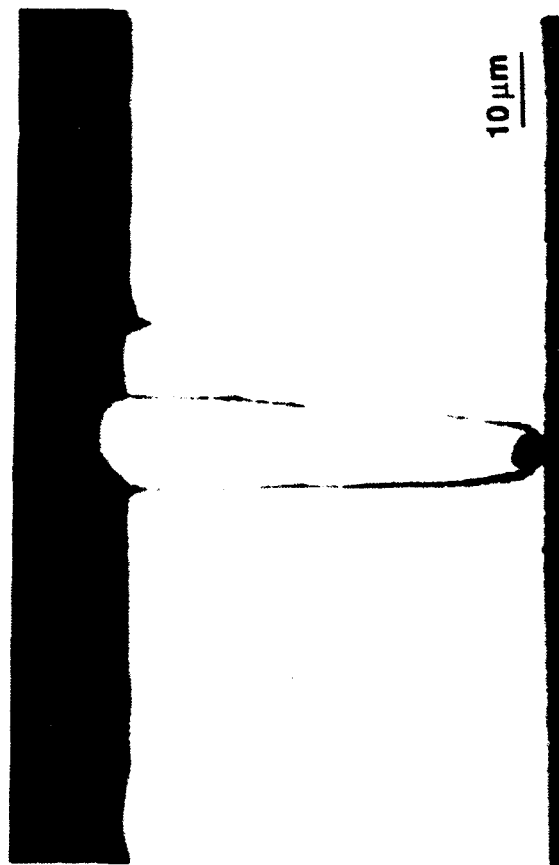


Figure 3. Cross-section through a PVD specimen showing the effect of a small particle on the collector plate on the structure of the deposit.



Figure 4. SEM micrograph of a PVD specimen revealing a nodule and its influence on deposit structure.

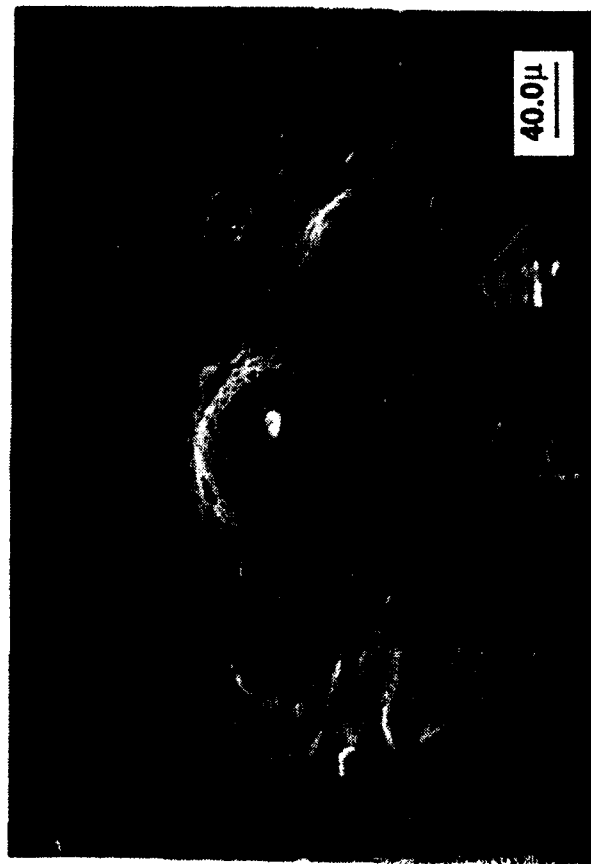


Figure 5. SEM micrograph of a PVD specimen showing the effect of a buried nodule on subsequent material growth.

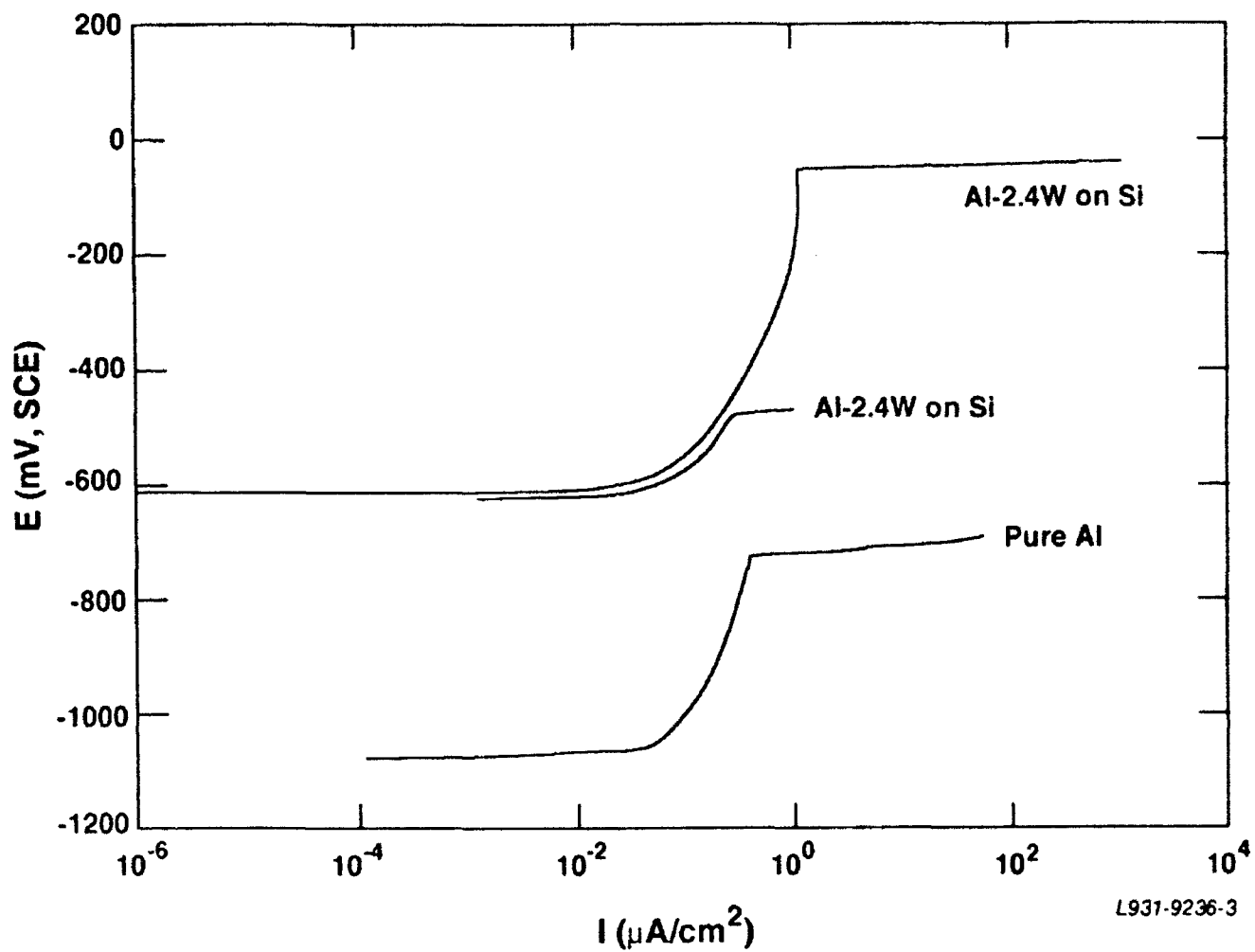


Figure 6. Replicate potentiodynamic scans of CD-12 specimens (Al-2.4W on Si) in 0.1M NaCl solution at pH 8 with a scan rate of 0.2 mV/s. Also shown for comparison is equivalent data for pure Al.

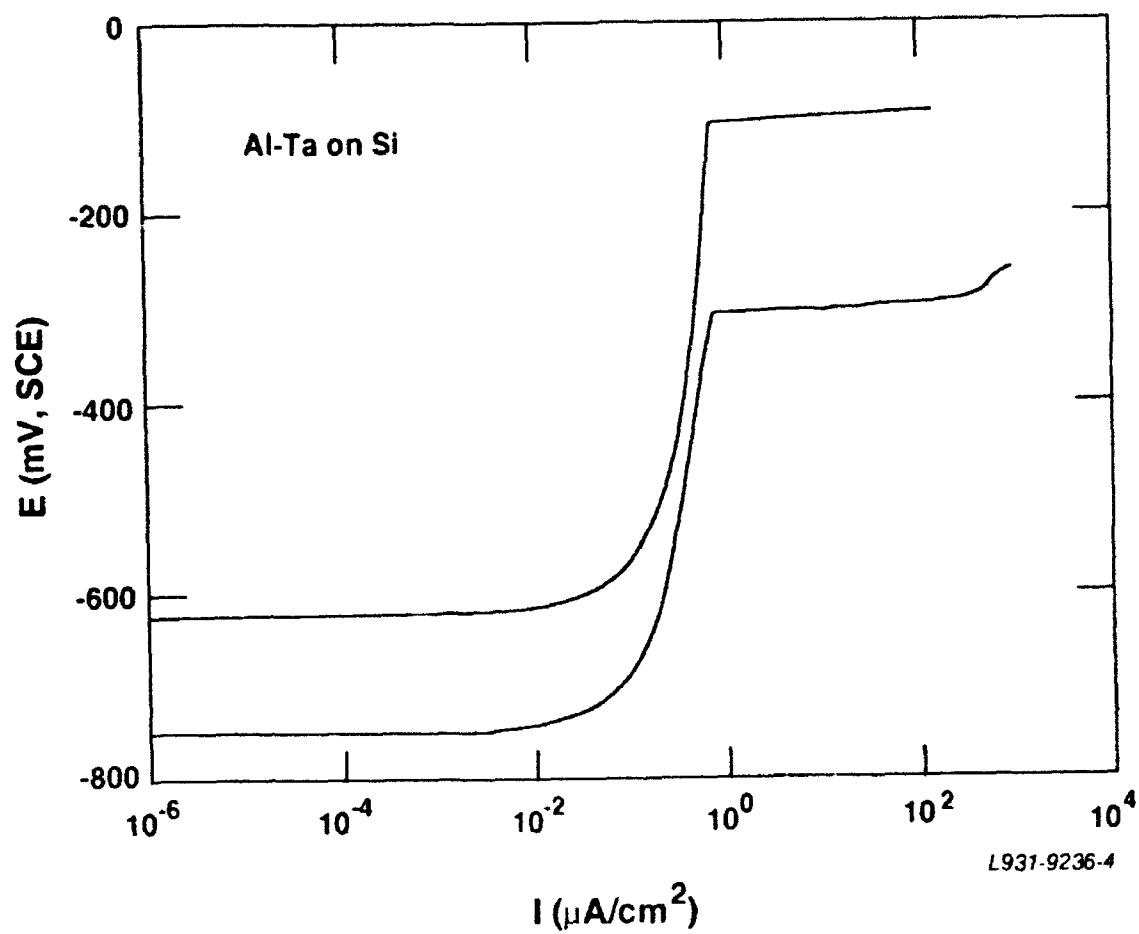


Figure 7. Replicate potentiodynamic scans of CD-13 specimens (Al-Ta on Si) in 0.1M NaCl solution at pH 8 with a scan rate of 0.2 mV/s.

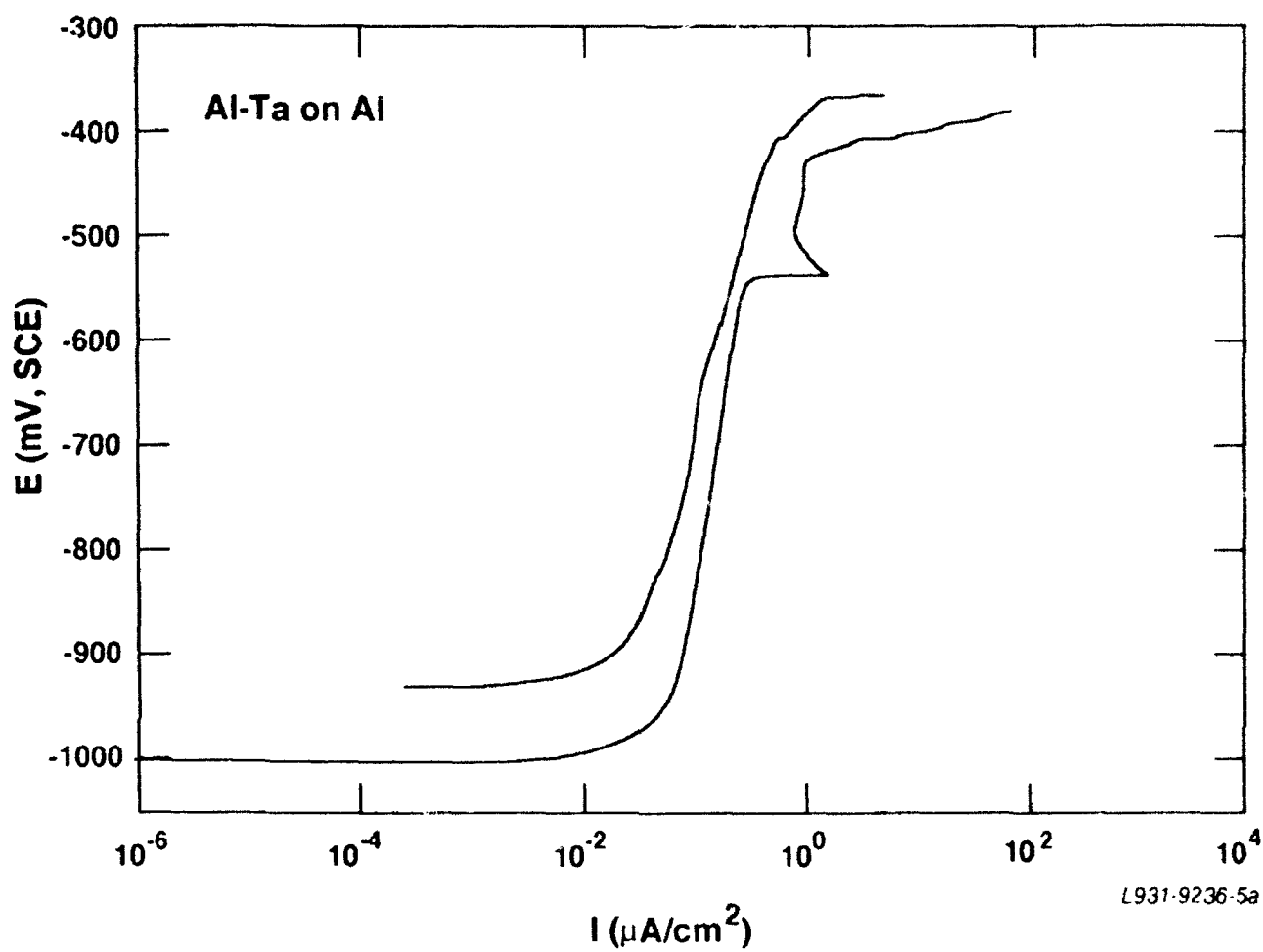


Figure 8. Replicate potentiodynamic scans of CD-16 specimens (Al-Ta on Al) in 0.1M NaCl solution at pH 8 with a scan rate of 0.2 mV/s.

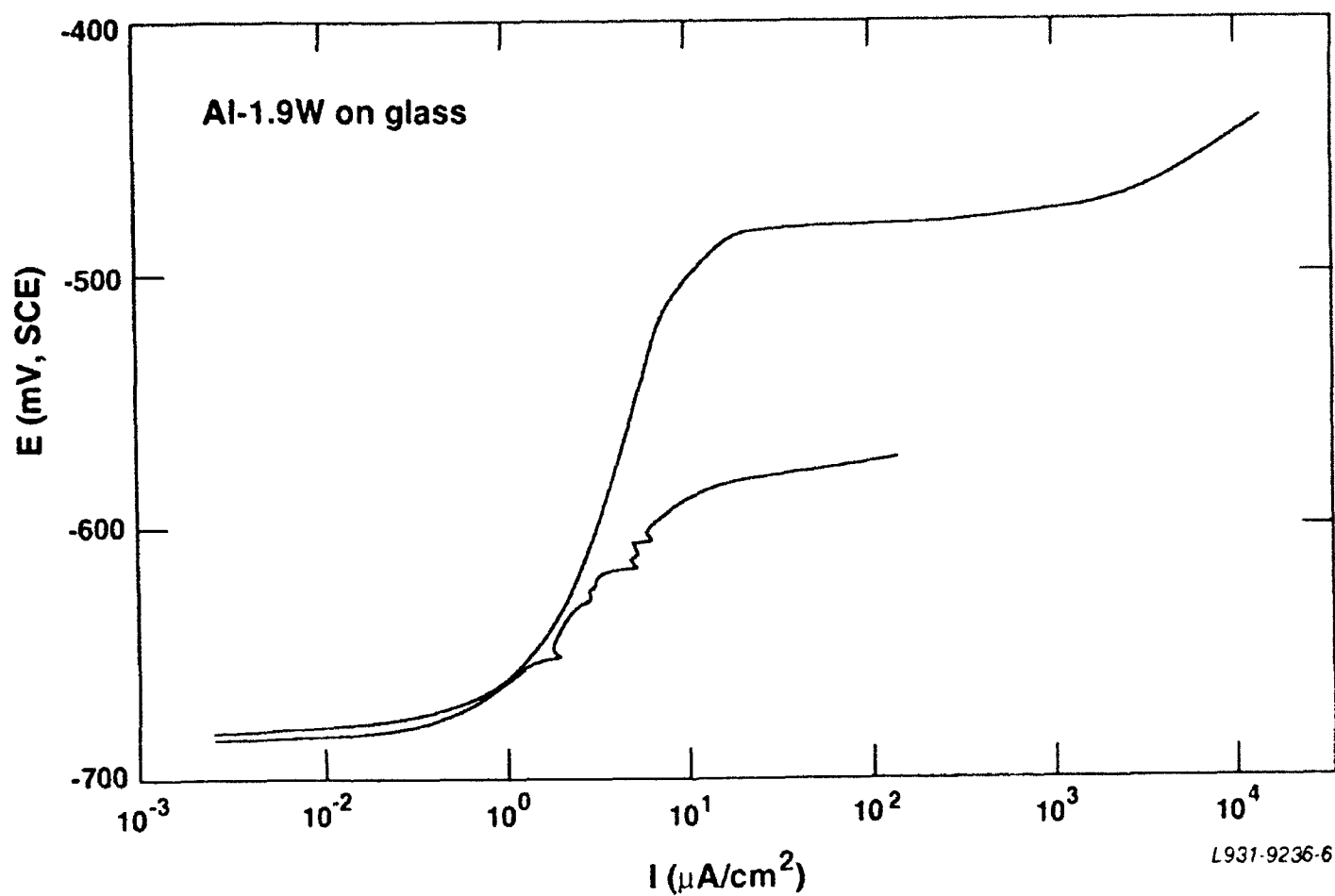


Figure 9. Replicate potentiodynamic scans of CD-17 specimens (Al-1.9W on glass) in 0.1M NaCl solution at pH 8 with a scan rate of 0.2 mV/s.

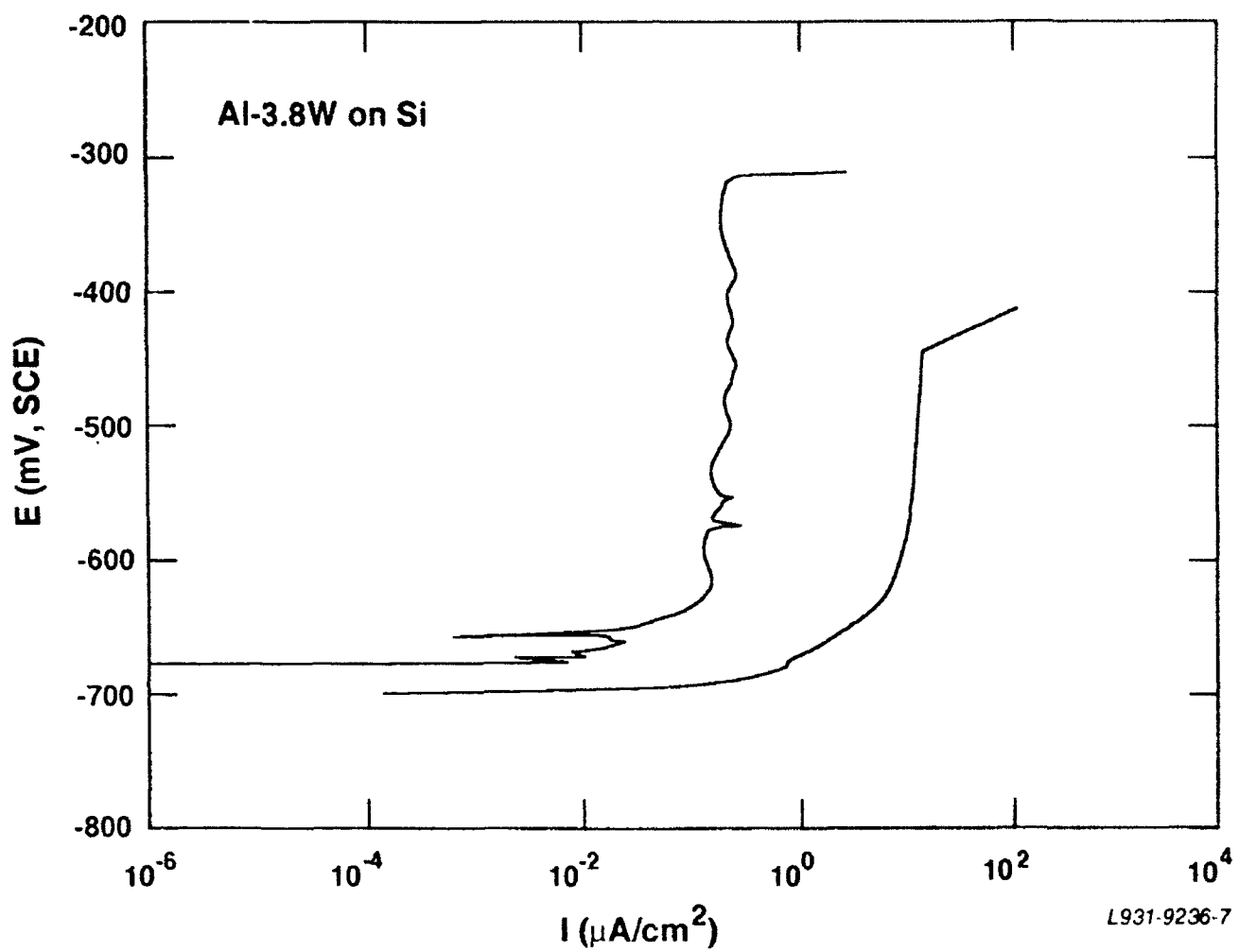


Figure 10. Replicate potentiodynamic scans of CD-25 specimens (Al-3.8W on Si) in 0.1M NaCl solution at pH 8 with a scan rate of 0.05 mV/s.

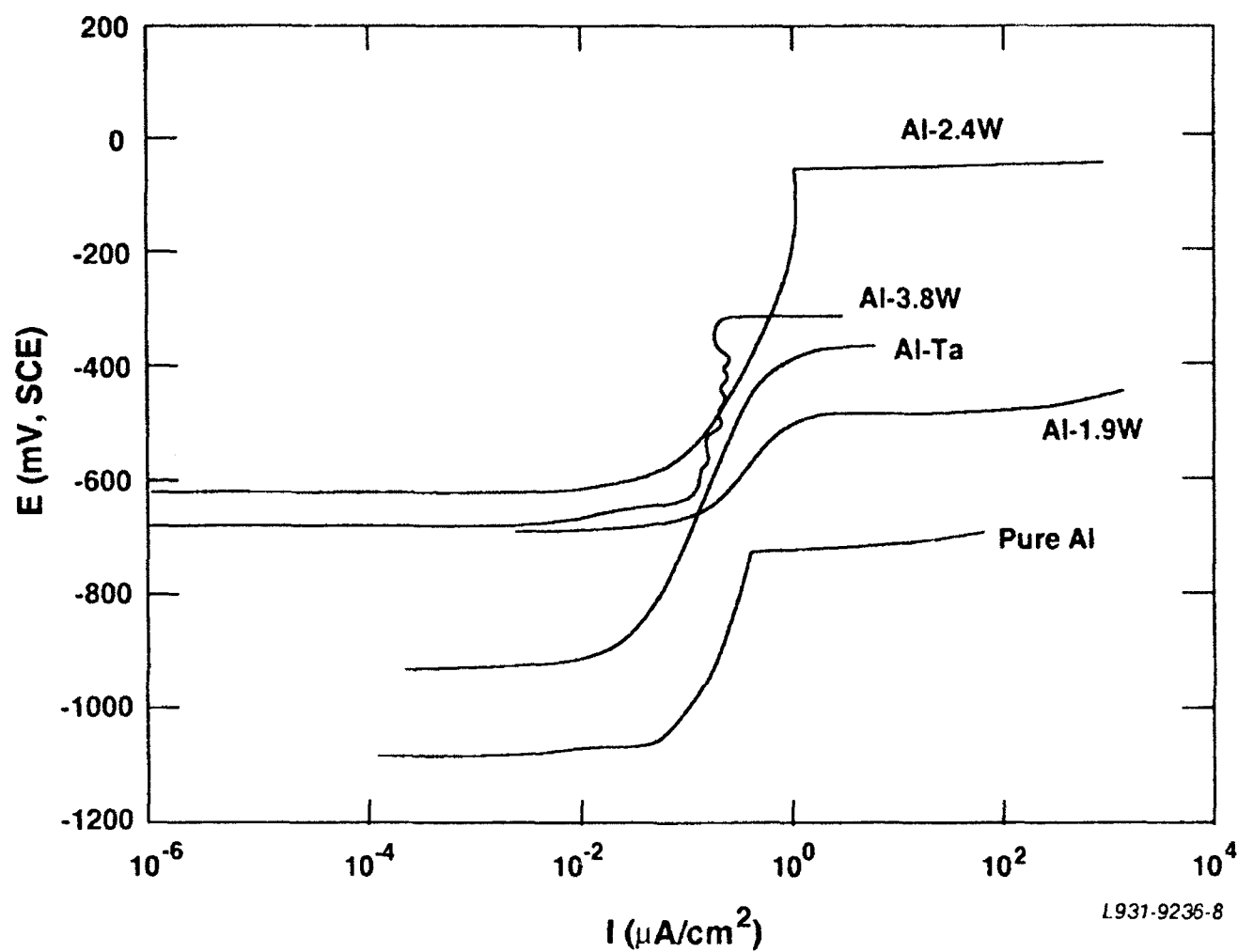


Figure 11. Comparison of potentiodynamic scans of all the vapor-deposited specimens and pure Al. All tests were in 0.1M NaCl solution at pH 8

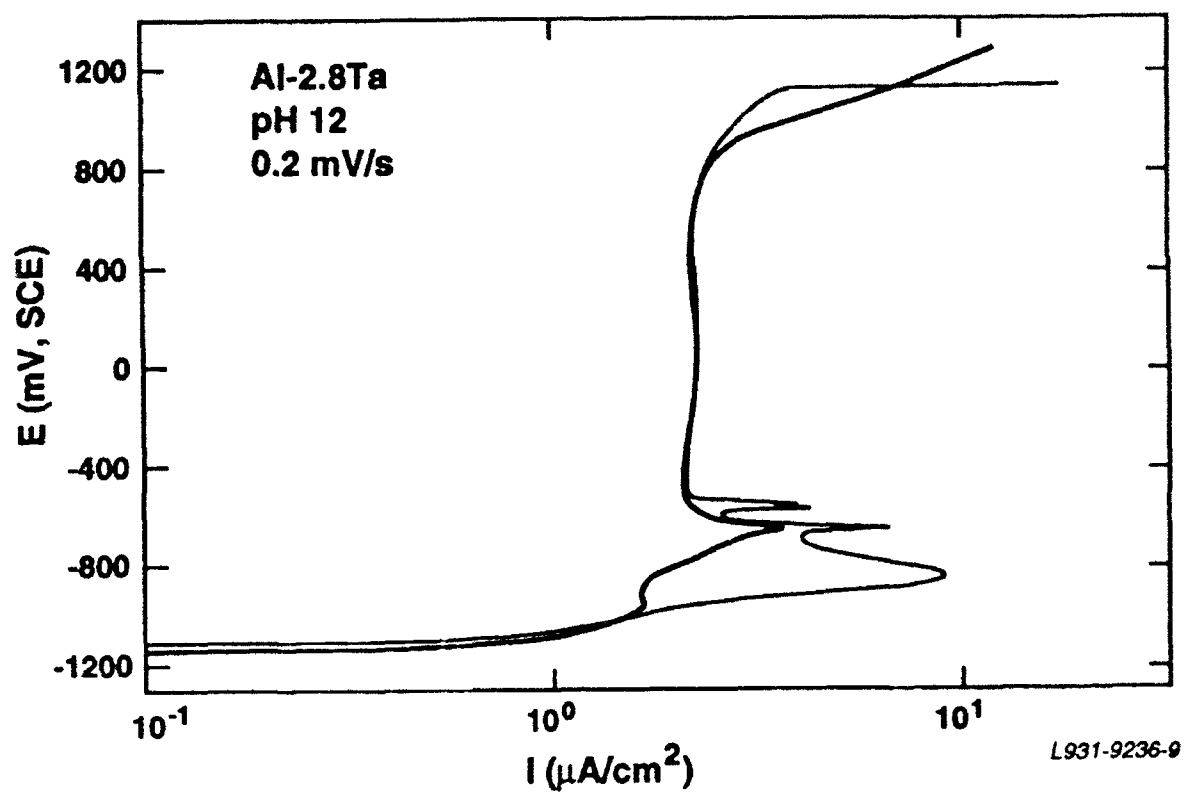


Figure 12. Replicate potentiodynamic scans of Al-2.8Ta specimens in 0.1 M NaCl solution at pH 12 with a scan rate of 0.2 mV/s.

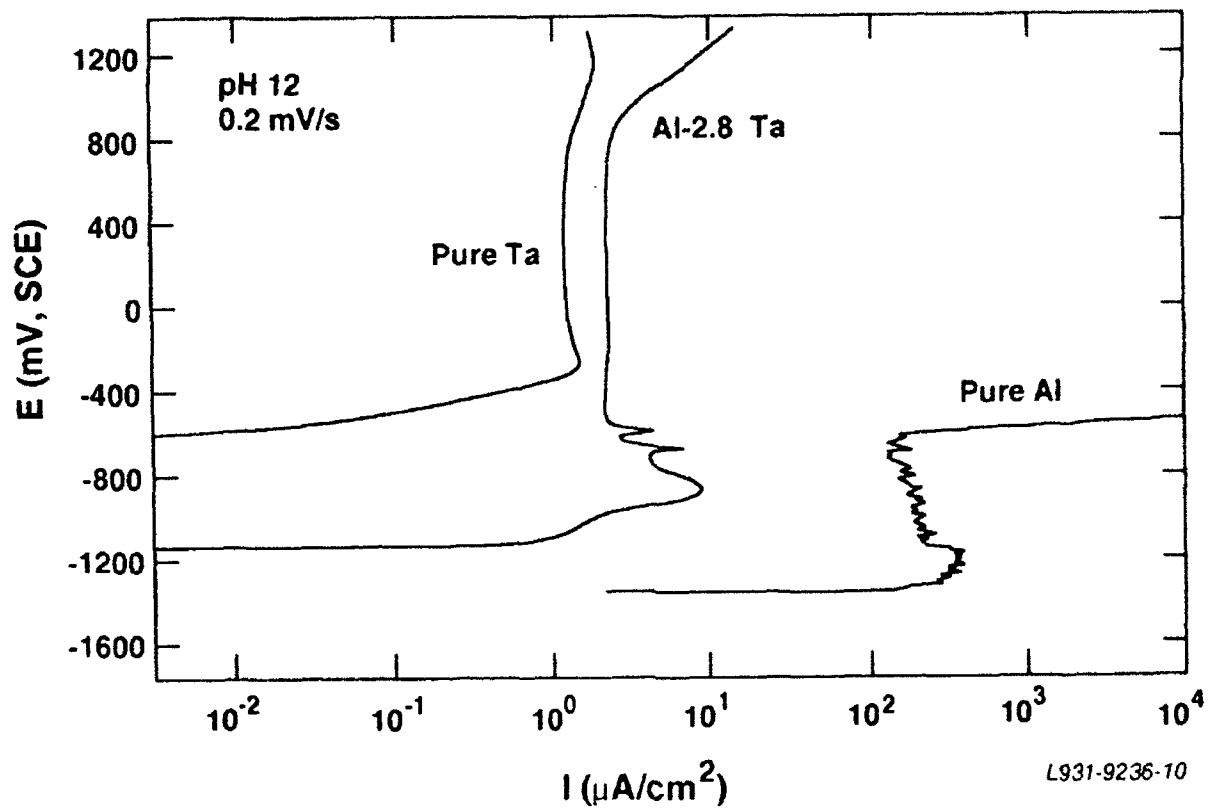


Figure 13. Comparison of potentiodynamic scans of Al-2.8Ta, pure Al, and pure Ta specimens in 0.1 M NaCl solution at pH 12 with a scan rate of 0.2 mV/s.

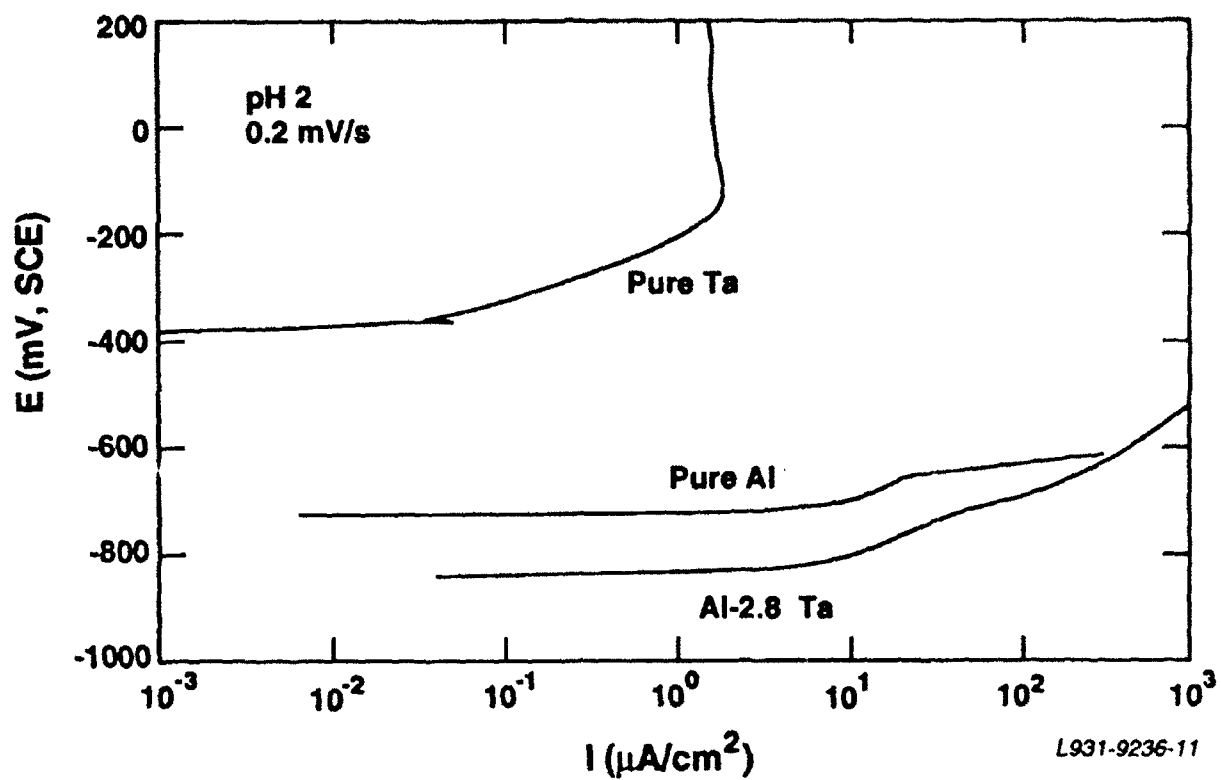


Figure 14. Comparison of potentiodynamic scans of Al-2.8Ta, pure Al, and pure Ta specimens in 0.1 M NaCl solution at pH 2 with a scan rate of 0.2 mV/s.

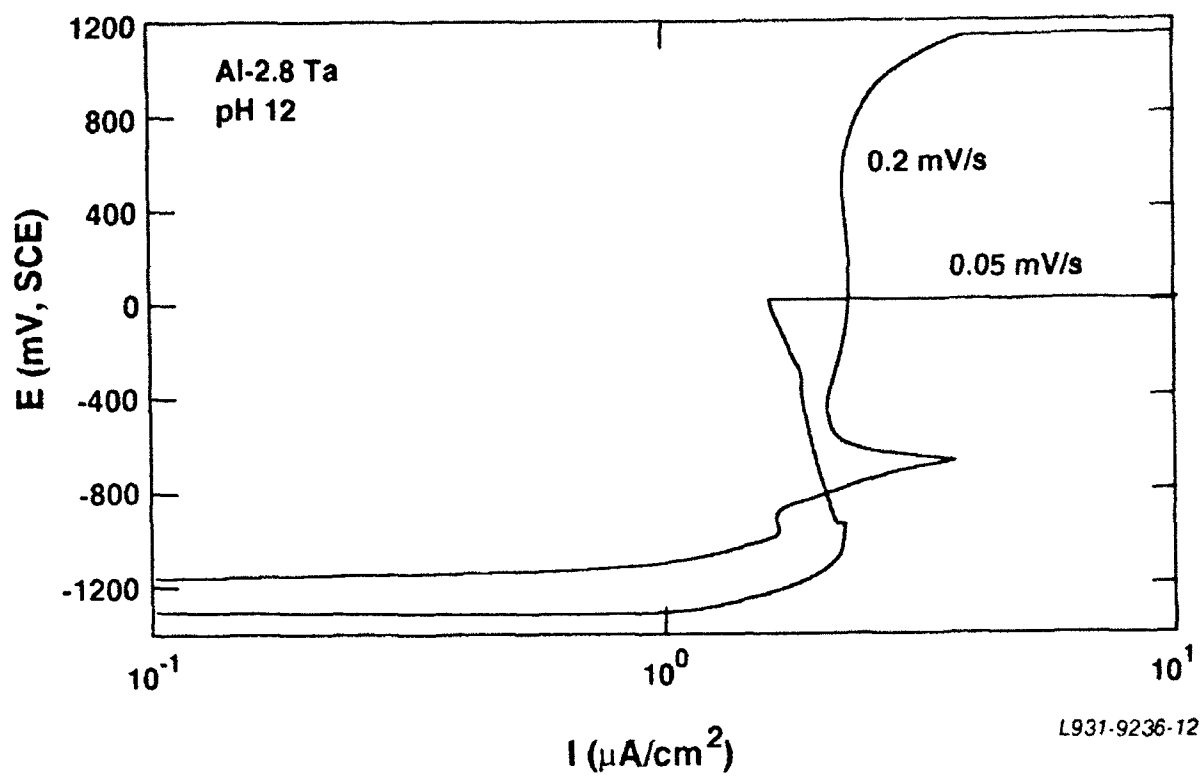


Figure 15. Comparison of potentiodynamic scans of Al-2.8Ta in 0.1 M NaCl solution at pH 12 with scan rates of 0.2 mV/s and 0.05 mV/s.

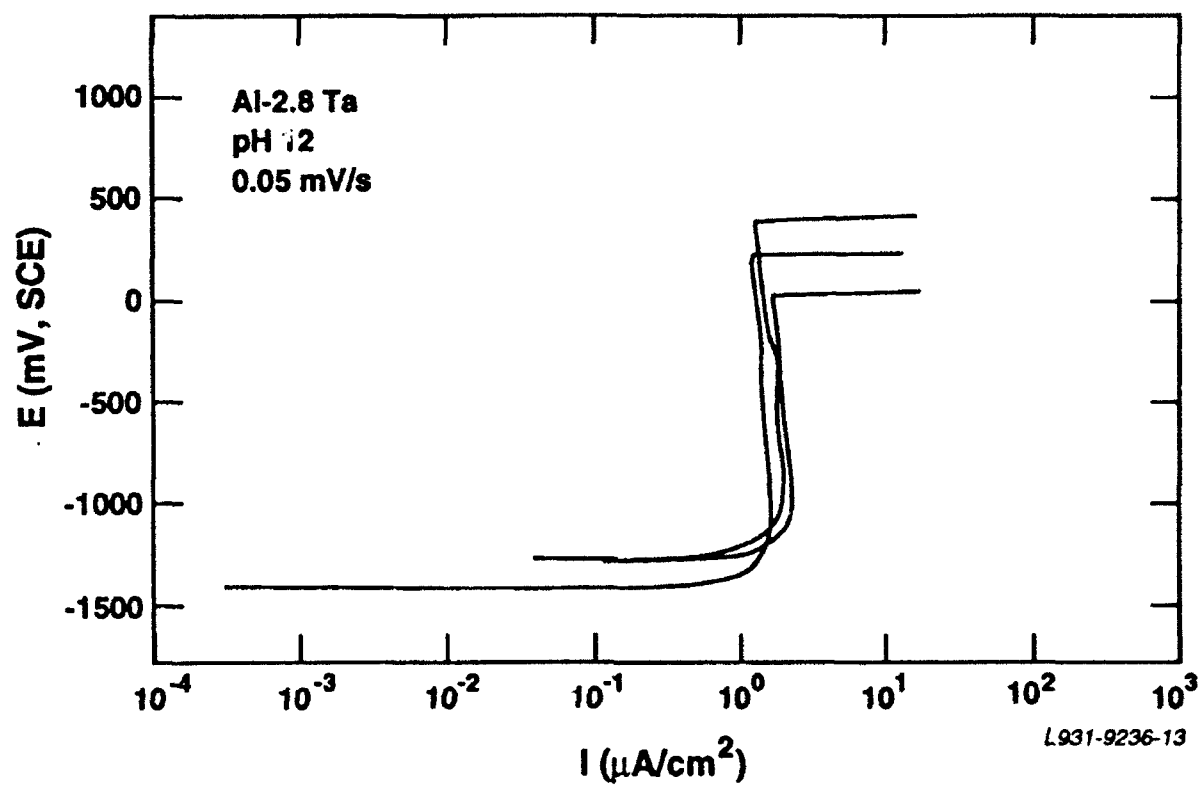


Figure 16. Replicate potentiodynamic scans of Al-2.8Ta specimens in 0.1 M NaCl solution at pH 12 with a scan rate of 0.05 mV/s.

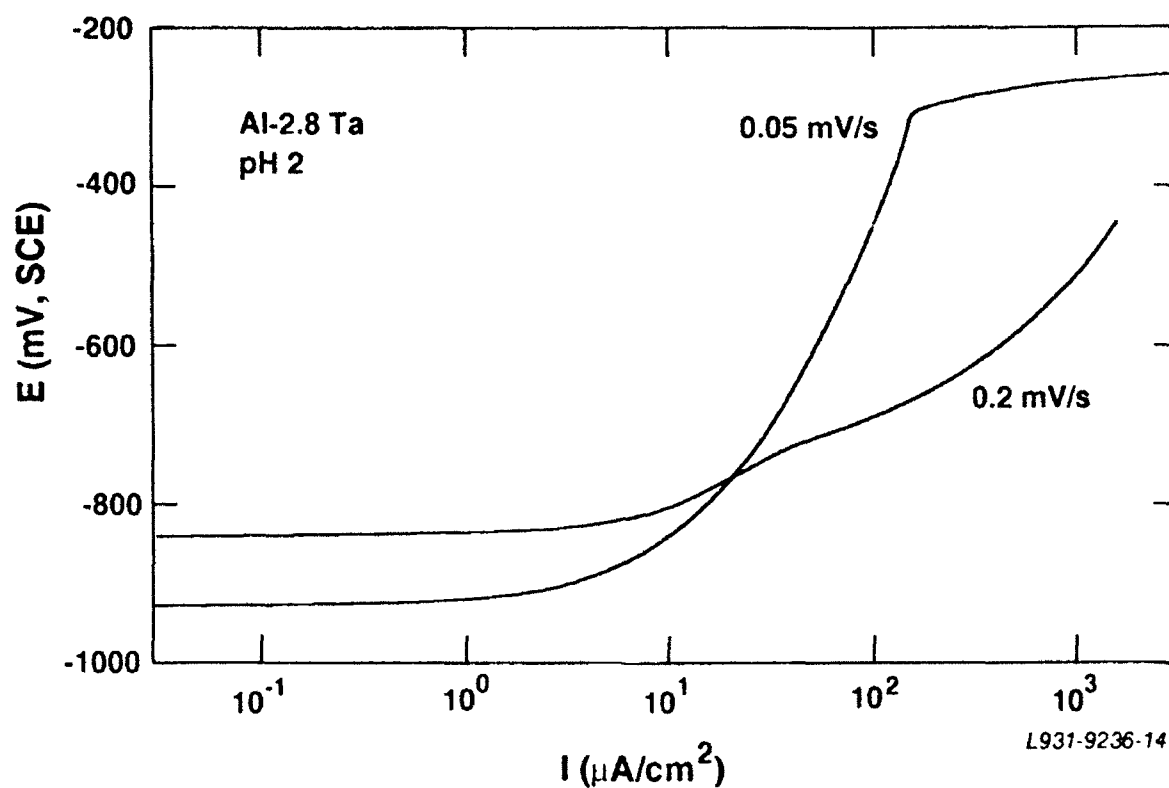


Figure 17. Comparison of potentiodynamic scans of Al-2.8Ta in 0.1 M NaCl solution at pH 2 with scan rates of 0.2 mV/s and 0.05 mV/s.

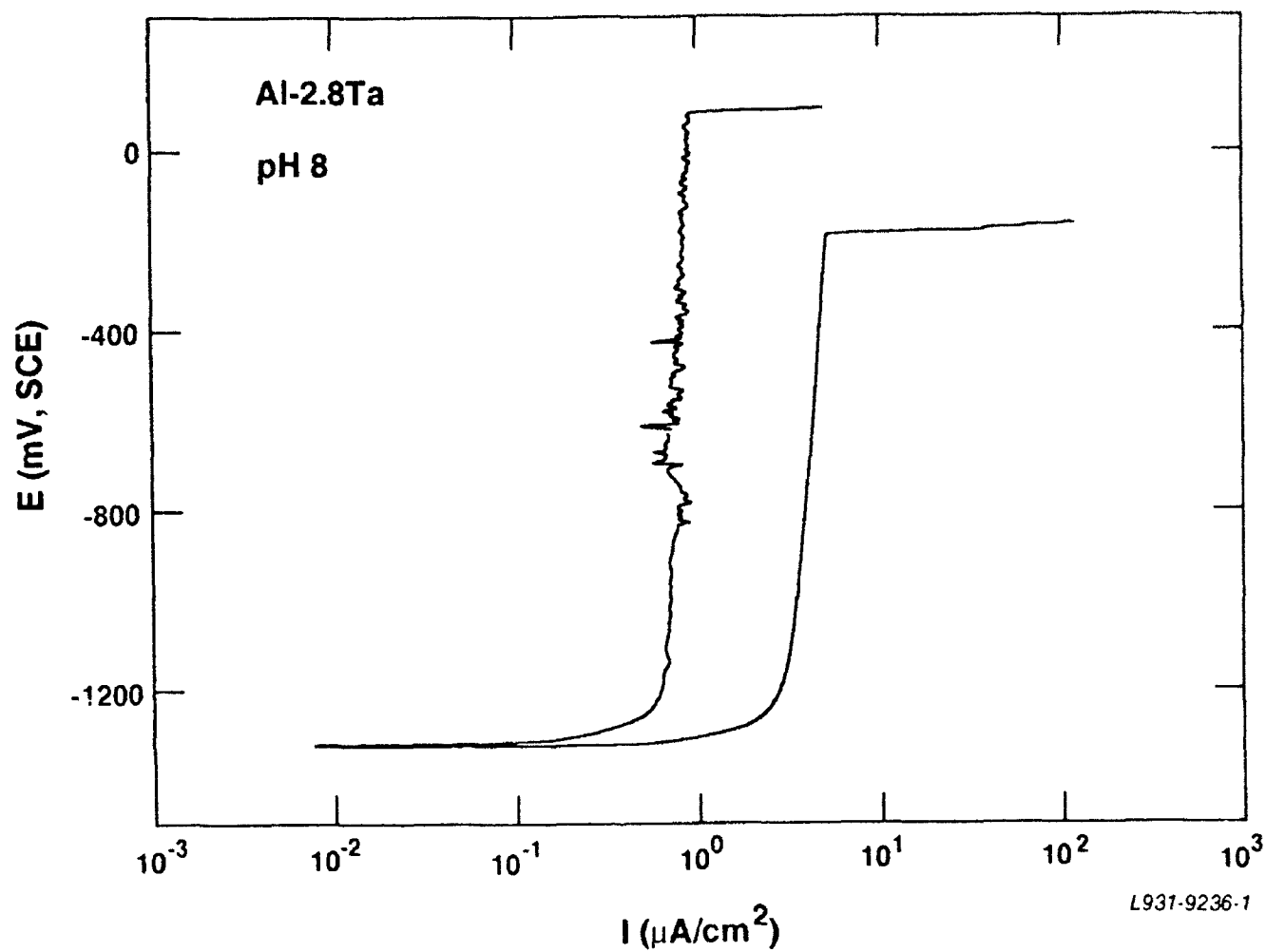


Figure 18. Replicate potentiodynamic scans of Al-2.8Ta specimens in 0.1 M NaCl solution at pH 8 with a scan rate of 0.05 mV/s.

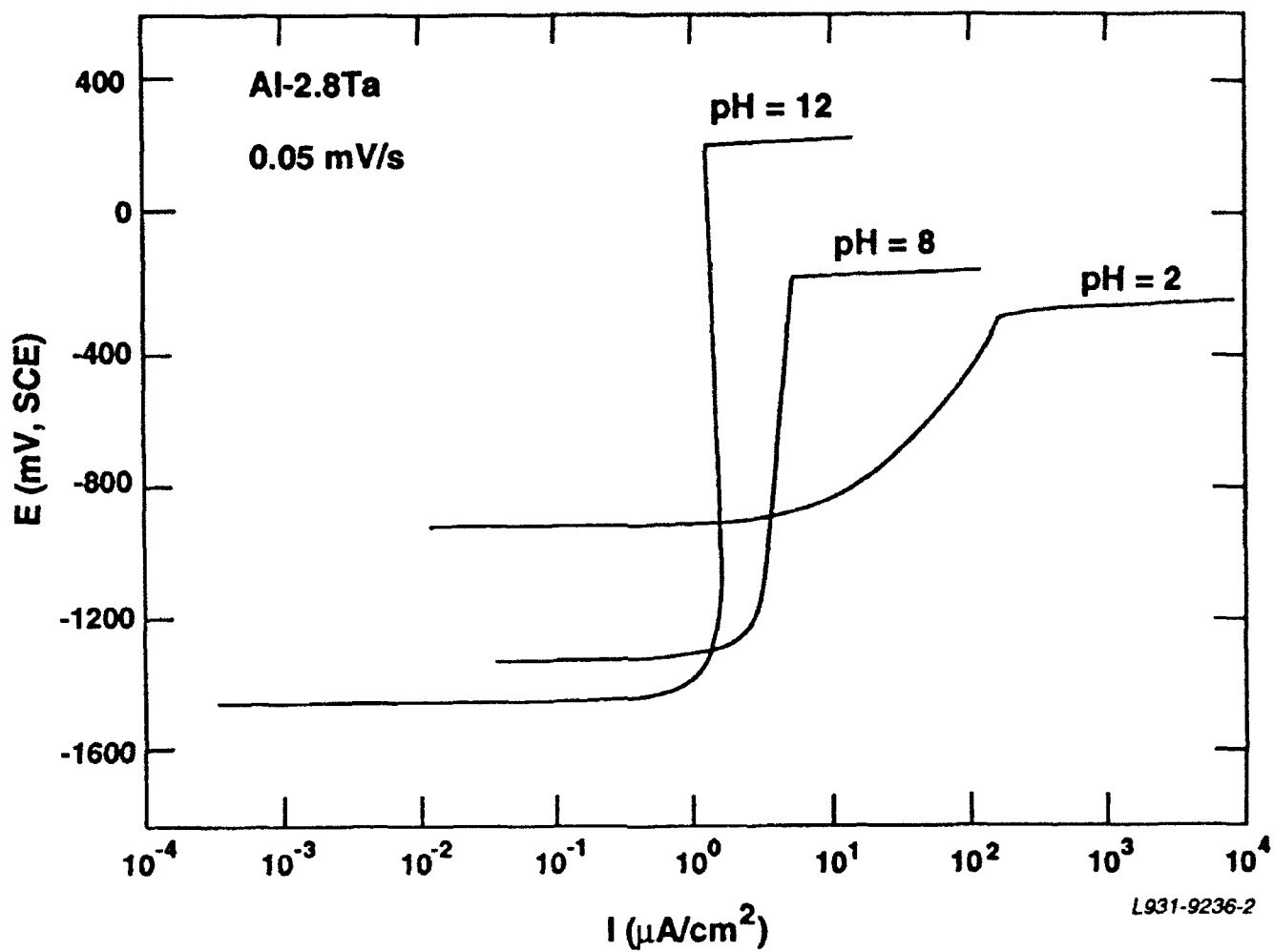


Figure 19. Comparison of potentiodynamic scans of Al-2.8Ta in 0.1 M NaCl solutions at pH 2, 8, and 12 with a scan rate of 0.05 mV/s.

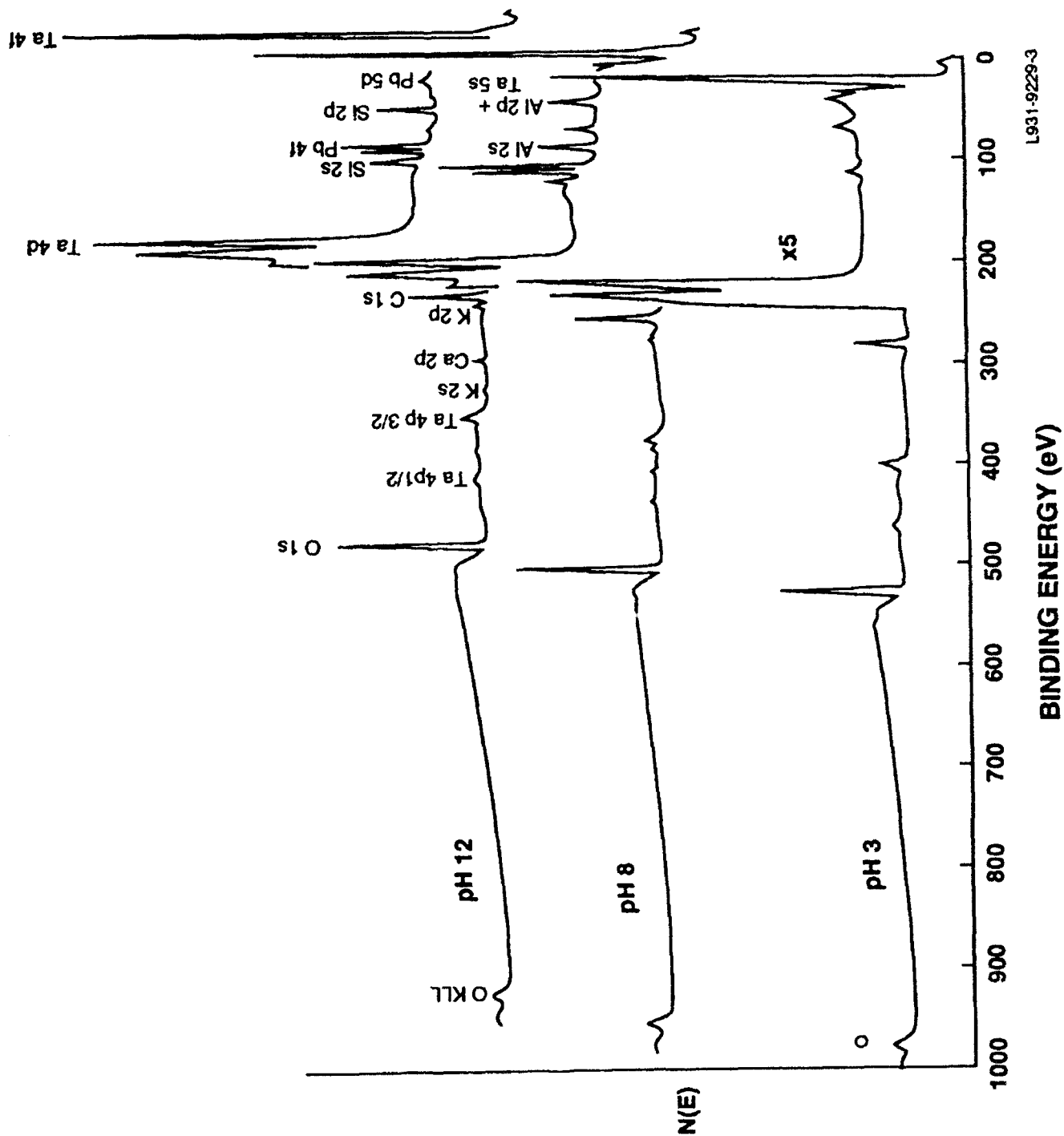


Figure 20. XPS survey spectra of Al-2.8Ta polarized to E_b in 0.1 M NaCl solutions at pH 2, 8, and 12. (The low binding-energy region of each spectrum was acquired with five times the number of scans of the remainder of the spectrum).

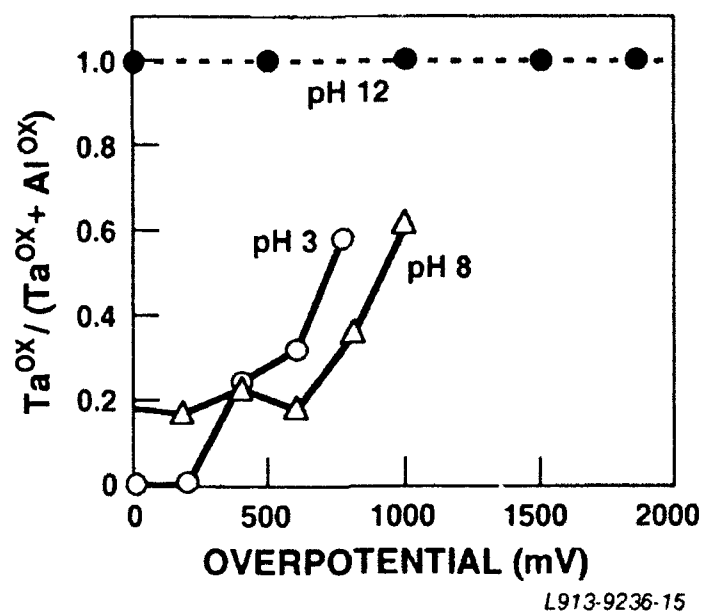


Figure 21. Ratio of oxidized Ta to all oxidized cations in the passive film, as measured by XPS, as a function of overpotential in 0.1 M NaCl solutions at pH 2, 8, and 12.

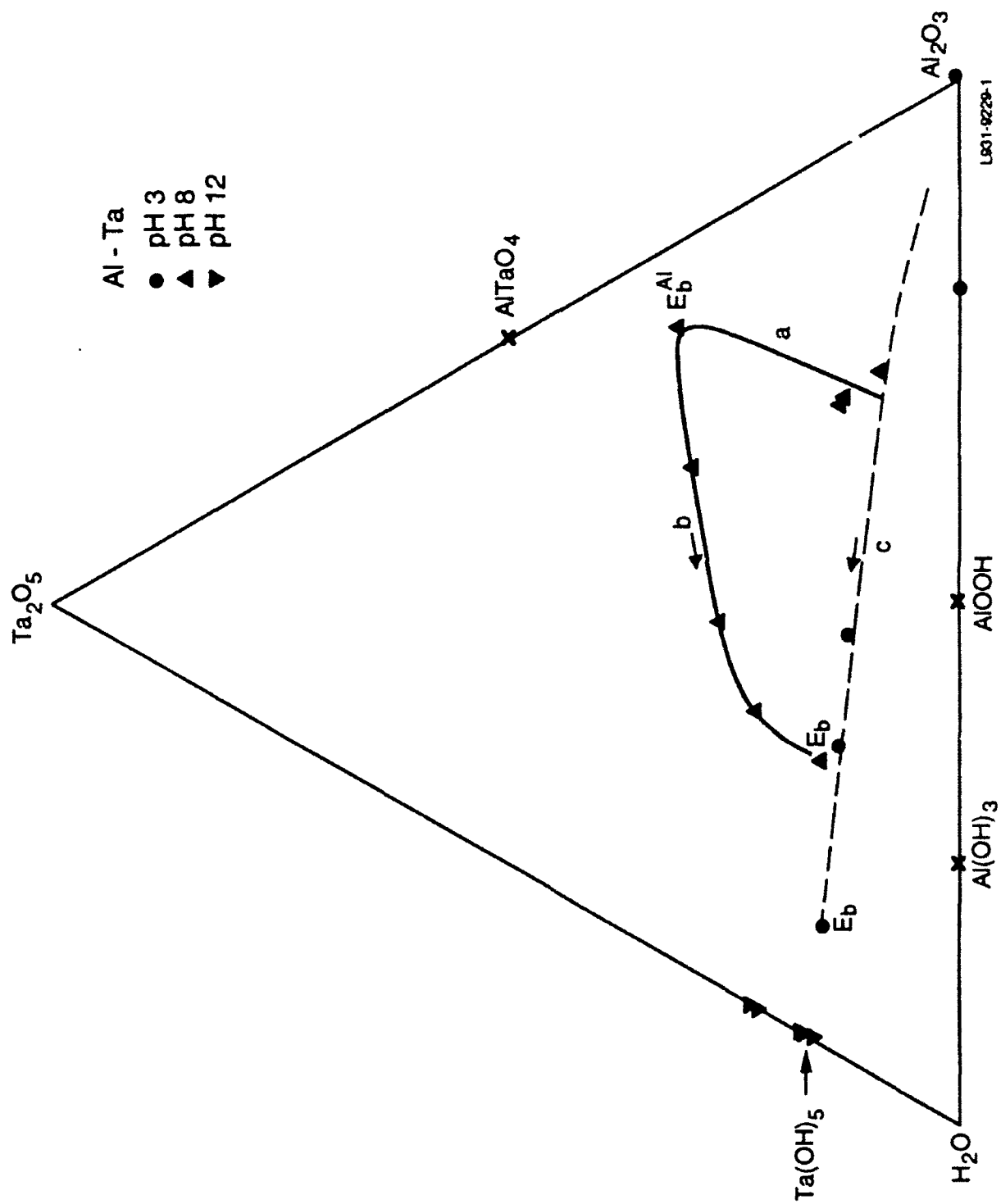


Figure 22. Al_2O_3 - Ta_2O_5 - H_2O surface behavior diagram showing the evolution of the passive film chemistry of Al-2.8Ta during polarization in 0.1 M NaCl solutions at pH 2, 8, and 12.

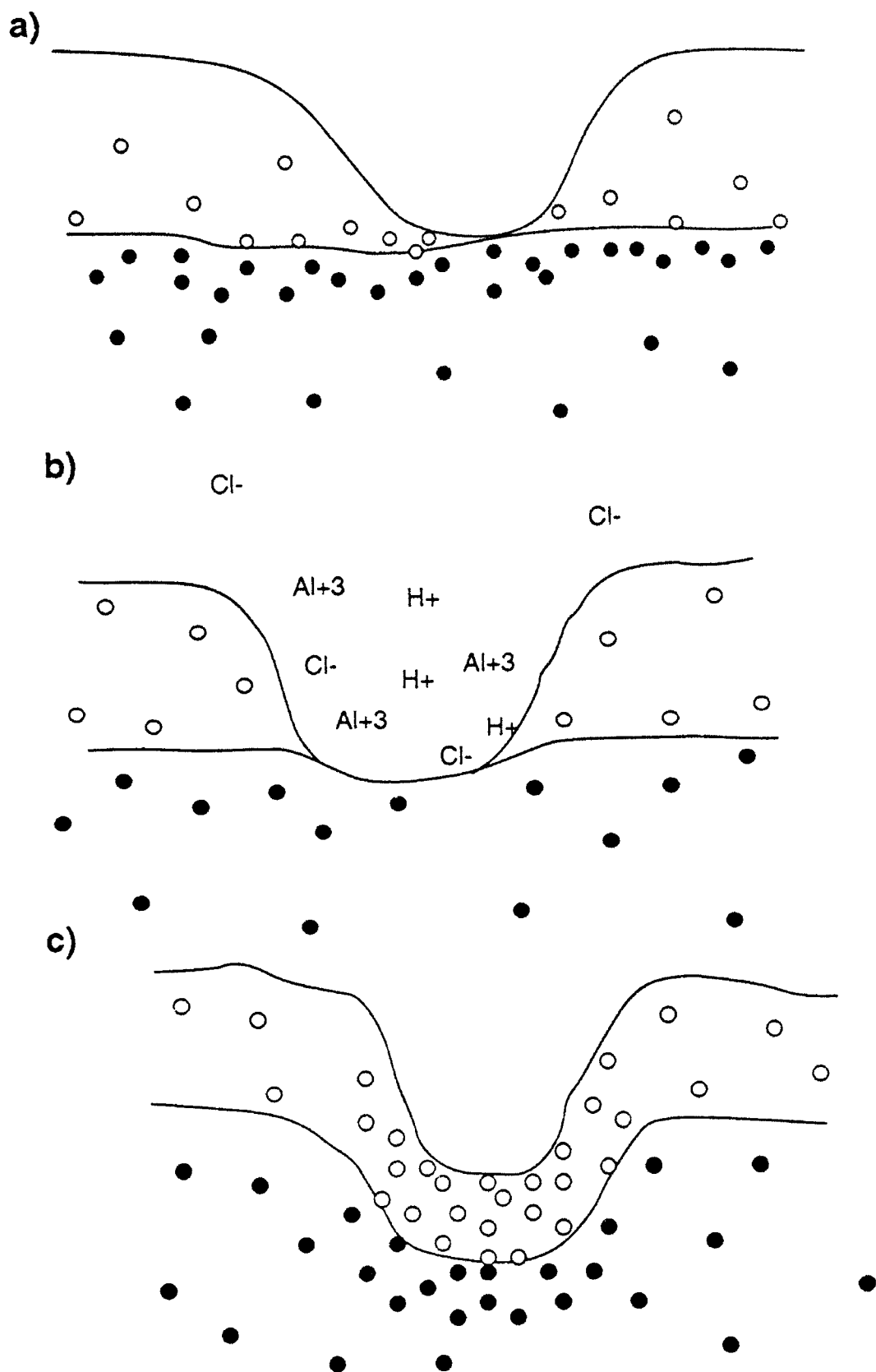


Figure 23. Schematic representation of the Solute-Rich Interphase Model (SRIM). a) Solute-rich metallic region under the passive film inhibits pit formation at defects. b) Acidification of an occluded cell and dissolution of Al causes the passive film and underlying alloy to become solute-rich locally. c) Solute-rich interphase passivates the cell due to more stable film and reduced adsorption of Cl^- . Solid circles correspond to metallic solute; open circles correspond to oxidized solute (Ref. 9).